UCLouvain

epl

École polytechnique de Louvain

Method to dimension HASEL actuators with antagonistic actuation

Author: **Clément Deckers**
Supervisor: **Renaud Ronsse**
Readers: **Thomas Pomponio, Laurent Francis**

Academic year 2025–2026
Master [120] in Electro-mechanical Engineering

Abstract

Hydraulically Amplified Self-healing ELectrostatic (HASEL) actuators are a new kind of artificial muscles developed over the past few years. Their mechanical properties as well as their compliance make them the perfect tool to be used in bio-mimecry application. This master thesis proposes a way to dimension those muscles for an antagonistic application. Grid Search (GS) and Competitive Multiple Objective Particle Swarm Optimization (CMOPSO) algorithms were used to find the most suited geometrical parameters respecting specifications of torque, range of motion and stiffness. The results found were then plot in a 3D space minimizing the mass and geometry of the actuators, analyzed and put in perspective with respect to what existing HASEL actuators are capable of.

Acknowledgment

This work would not have been possible without the help of certain people whom I would like to thank.

First, I would like to thank Pr. Ronsse for his time and guidance throughout this master thesis. His advice proved to be valuable and helpful.

Next, I am sincerely grateful to Ph.D. student Thomas Pomponio for his assistance and willingness to answer my questions. He has always taken the time to help me improve the quality of my work and to share his knowledge with me.

I would also like to thank my friends, who helped me throughout this project and supported me as best they could.

Finally, I would like to thank my family for their unwavering support, their valuable advice, and their constant encouragement

AI disclaimer

Gemini was used in this document as a consultant to help improve the quality of the text (spelling and syntax) and the quality of some figures. In particular: Fig. 5.4 was enhanced using AI.

Acronyms

PAM Pneumatic artificial muscle

DEA Dielectric Elastomer Actuators

HASEL Hydraulically Amplified Self-healing ELectrostatic

SMA Shape memory alloy

GS Grid Search

PSO Particle Swarm Optimization

NSGA-II Non-dominated Sorting Genetic Algorithm II

CMOPSO Competitive Multiple Objective Particle Swarm Optimization

BOPP Biaxially Oriented Polypropylene

PVDF Polyvinylidene fluoride

List of Figures

List of Tables

Contents

Chapter 1

Introduction

Soft robotics has been a growing field in engineering for the past few years. Several technologies have been developed, including electrostatic actuator like Dielectric Elastomer Actuators (DEA), fluid-driven actuators, thermally responsive actuators and magnetically responsive actuators[11, 24, 31].

Among them, a new kind of soft actuator was introduced in 2018: Hydraulically Amplified Self-Healing ELectrostatic actuators or HASEL actuators. HASELs hold great promise as they combine advantageous characteristics of existing soft actuators while compensating for their limitations.

While several application regarding HASEL technology have already been demonstrated [25], their biomimetic potential remains to be fully explored. This master's thesis proposes to investigate HASEL actuators in an antagonistic configuration. This configuration enables independent control of both torque and stiffness at the joint depending on the contraction level of the muscles involved [13]. In particular, this work aims to address the following questions: how does the geometry of HASEL actuators influences the performance of an antagonistic configuration and is there a method to determine an optimized geometry for this application?

To answer these questions, Chapter 2 presents a literature review on soft actuators providing an overview of the field and the working principles of HASELs. Then, Chapter 3 introduces the antagonistic configuration along with its associated constraints and physical limitations. Afterwards, Chapter 4 describes the methodology followed and the algorithms implemented. Chapter 5 presents the results obtained and discusses their significance. Finally, Chapter 6 addresses potential improvements and conclude this master's thesis.

Chapter 2

State of the art

This chapter proposes a literature review on soft actuators and HASEL technology. It begins with a brief presentation on soft actuation development throughout the years before comparing the different technologies used nowadays. Then, it describes HASELs actuators with more details before focusing on Peano-HASEL and an analytical model developed by Kellaris et al. [16].

2.1 Development of soft actuators

Classical actuators are made of three parts: a motor to generate the power, a transmission mechanism and an end effector that performs the task it was designed for. While this system presents significant advantages such as high precision, robustness and controllability it also exhibits several limitations. These actuators are not able to adapt easily to their environment and they do not offer safe human-robot interaction. Moreover, regarding the task that needs to be performed, they can show inefficiencies regarding power consumption and weight.

To address these issues an alternative kind of actuators called soft actuators based on biological behaviors was developed. In contrast with rigid mechanisms, soft actuators integrate a deformable element that allows displacement from the equilibrium position when an external force is applied to the actuator [12]. From a practical point of view, this actuator allows for safer human-robot based interactions as they are more compliant than their rigid counterparts. Moreover, this compliancy allows them to adapt to their environment as they are able to modulate their rigidity depending on the situation.

In the 20th century, several ideas and developments were imagined and prototyped. In 1957, McKibben developed Pneumatic artificial muscle (PAM) which is considered as the first artificial muscle, a soft actuator for which both the elastic and actuation function are embedded in the same element [20]. Later on, in the 1990s, with the development of soft materials such as polymers and elastomers scientists expanded the idea of bio-inspiration and thought of new kinds of soft actuators mimicking animal and human behaviors.

Between 2011 and 2013, George Whitesides and his team, explored the idea of a flexible robot inspired from an octopus [30]. This led, in 2016, to the first entire soft actuator, relying only on chemical reaction to move [29]. This last work in particular was considered as a major breakthrough in the field of soft actuation. Finally, in 2018 Kellaris et al. proposed a new kind of soft actuator: HASEL artificial muscle, an electrically responsive actuator inheriting properties from both DEA and hydraulic actuators while also compensating for their weaknesses.

2.2 Review of soft actuators

Figure 2.1 from Perera et al. [23] illustrates the variety of soft actuators currently available. They have been classified by their input stimulus.

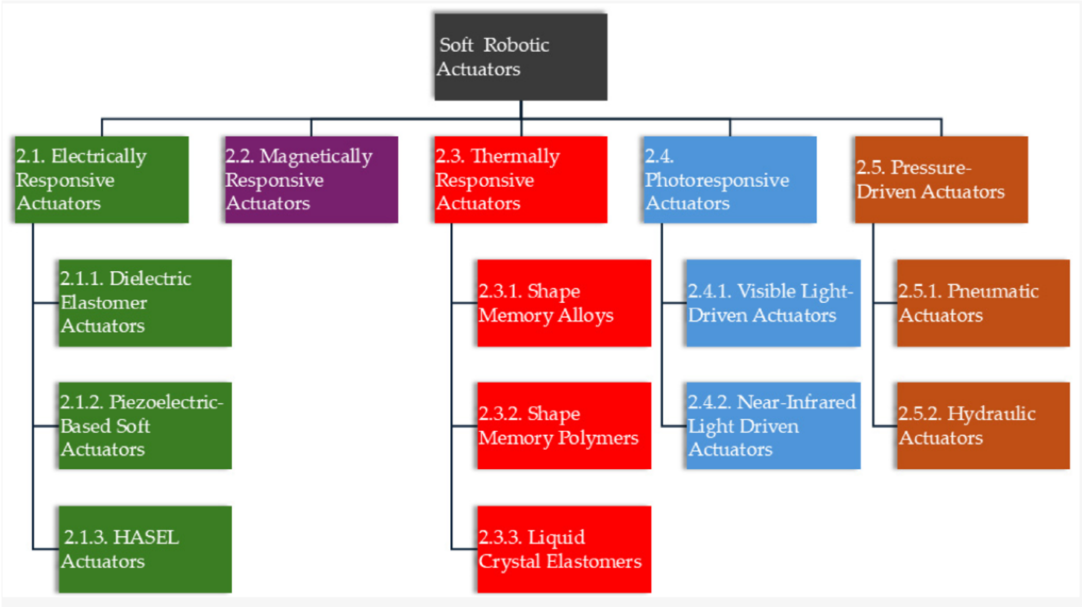

Figure 2.1: Classification of soft actuators [23]

2.2.1 Pressure-Driven actuators

Pressure-Driven actuators achieve motion and deformation through control of fluidic pressure inside inflatable cavities such as the one depicted in Fig. 2.2a from Yasa et al. [31]. They are composed of elastomeric materials coupled with inextensible layers used to guide the deformation. A pump compresses and decompresses the fluid (usually air or water) inside the inflatable cavities.

This technique allows for various kinds of geometries depending on the motion and the deformation rate to be achieved. It also generates high forces and does not require a continuous power consumption (as a valve can be closed to maintain the cavities inflated). In contrast, it is hard to control the motion accurately and it cannot sustain high payloads. Moreover, a tear in the elastomeric membrane of one of the cavities can lead to a complete failure of the system.

The most famous pressure-driven actuators are PAMs. Nowadays, they are mainly used in the robotic actuation field where low power-to-weight ratio and compliance are important such as walking or running robots. Moreover, hydraulically actuated McKibben muscles have also been used for underwater applications [7, 32].

2.2.2 Thermally responsive actuators

These soft actuators are mainly based on Shape memory alloys (SMAs). These alloys are temperature-sensitive metallic composite materials. Once deformed, they present the interesting effect of being able to go back to their original (pre-deformed) state when a certain temperature called transformation temperature is applied to them[31]. This temperature is often applied through a resistor by Joule heating (see Fig. 2.2b). The main advantage of such actuators is their ability to deform. In a straight configuration they can deform by up to 8 % and in spiral, this deformation can reach up to 300% [19]. In addition, they can work with low voltage stimulation and silently. Their electric stimulation makes them predisposed to work underwater where they can benefit from an enhanced actuation speed and an increased cooling rate. However, they require to be tethered. Furthermore, since they rely on temperature changes to actuate, the energy efficiency of these devices is significantly lower compared to other technologies. Other drawbacks to consider are their high hysteresis and non-linear nature making them harder to control.

2.2.3 Magnetically responsive actuators

Soft actuators using magnetic response are composed of microscopic ferromagnetic materials integrated into soft elastomeric matrices [34]. When a magnetic field B is applied, each magnetic domain of these microscopic materials spatially aligns itself with the field (see Fig. 2.2c). This spatial alignment is the key factor to play with in order to obtain the desired soft body, deformation and motion[31]. Due to their high controllability and precision, these kinds of actuators are usually well-suited for surgical purposes and especially in complex environment requiring extra caution such as the brain. Recently, a magnetically responsive hydrogel actuator was developed to treat heart disease[3]. However, they need complex equipment to control the magnetic field and as the magnetic field strength decreases with the distance, the use of this kind of actuator remains limited.

2.2.4 Photo-responsive actuators

Under the stimulus of light, these devices can convert light energy into mechanical motion. The main advantage lies in the capability to remotely control the actuator, making it suitable for wireless or underwater actuation [31]. However, their practical implementation remains constrained by relatively low actuation forces, slow response times, and a strict requirement for a clear line-of-sight between the light source and the active soft material. Photo-responsive actuators are divided into several categories depending on the wavelength of light that triggers them. The most common are visible light actuators (see Fig. 2.2d) and near-infrared actuators.

2.2.5 Electrically responsive actuators

Electrically responsive actuators are divided into three categories: Piezoelectric-Based Soft Actuators, Dielectric Elastomer Actuators DEA and Hydraulically Amplified Electrostatic actuators or HASEL actuators.

Piezoelectric-Based Soft Actuators

These actuators are based on the piezoelectric effect, which denotes the property of certain materials to generate a voltage or an electric charge when a mechanical force is applied or reciprocally, to produce a mechanical deformation when an electric field is applied. They offer the following benefits: fast response, high precision, light weight and high actuation frequency. However they suffer the following drawbacks: limited strain, low blocking force and the need for high electric fields leading to high power consumption.

Usually used as sensors, the piezoelectric technologies have also found their way into assistive gloves for rehabilitation purposes [4].

Dielectric Elastomer Actuators DEAs

DEAs are made of compliant electrodes separated by a layer of dielectric material. When a voltage is applied to these electrodes, a Maxwell stress is generated compressing the dielectric material and pushing the electrodes closer to each other [32]. This results in the dielectric material deformation as depicted in Fig. 2.2e. In particular, this capacitor structure allows for significant deformation ($> 100\%$)[25]. However, to achieve these high strains, these actuators need prestretch and rigid frames. Furthermore, they require high operating voltages ($\sim$ kV) increasing the risk of dielectric breakdown. Their high energy density, self-sensing capabilities and significant strain make them suitable for biomedical applications such as artificial muscles.

Two types of DEAs opened the way for HASEL's invention: hydrostatically coupled DEAs in which dielectric liquid couples the deformation of multiple elastomer membranes and DEAs-based pumps in which electrostatic zipping of dielectric elastomer membranes onto rigid substrates is used to pump fluids[25].

Hydraulically Amplified Electrostatic actuators HASEL

Presented as a revolutionary development in the field of electrically responsive actuators [23], these actuators help to solve some of the shortcomings of DEAs by incorporating aspects of pressure-driven actuators such as high flexibility, versatility in motion and safe interaction with their environment. More specifically, their characteristics make them suitable for applications requiring precision, adaptability, and bio inspired motions, like soft grippers and prosthetics. The inherent flexibility and scalability of this technology provides opportunities for integration into complex and lifelike systems for which traditional actuators are not suited.

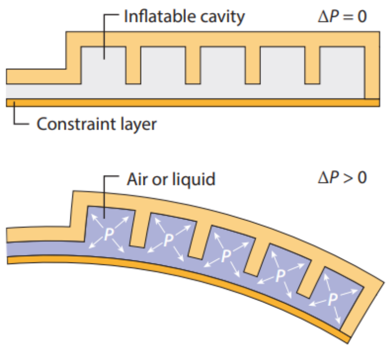

(a) Pressure-driven actuators principle [31]

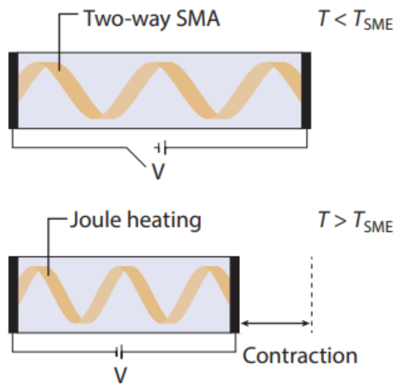

(b) Thermal actuators principle [31]

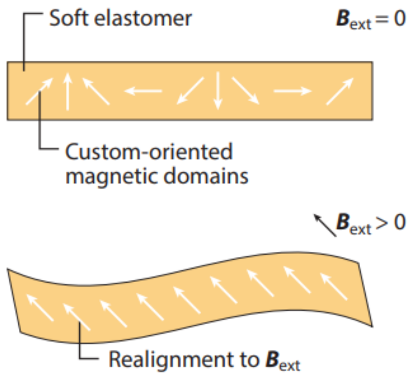

(c) Magnetic actuators principle [31]

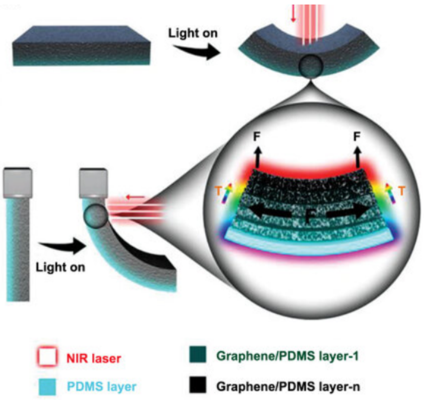

(d) Photo-responsive actuator principle [34]

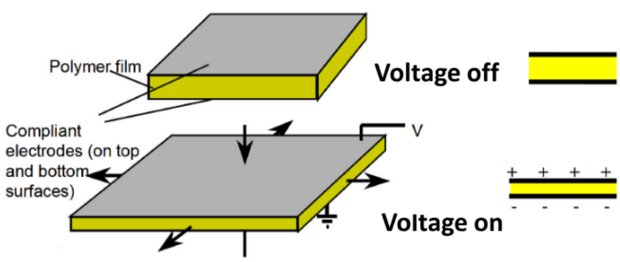

(e) DEA principle [32]

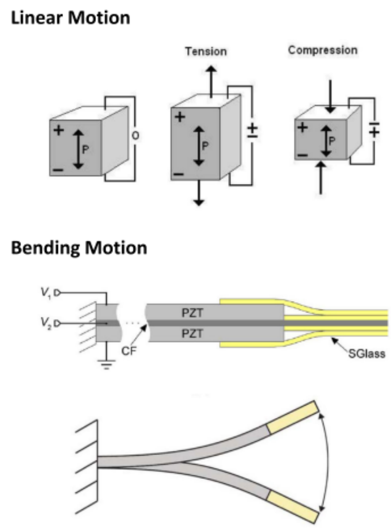

(f) Piezoelectric actuators principle [32]

Figure 2.2: Soft actuators technologies

2.3 Review of HASELs actuators

While the actuators described in Section 2.2 offer their advantages and disadvantages, HASELs actuators seem to compensate for the disadvantages of DEAs by using hydraulic technology. Over the years, several designs and geometries have been considered. Below are the most common ones. Two types of actuators can be distinguished. On one hand, the contracting actuators that achieve contraction of the shell through zipping of the electrodes under voltage application, and on the other hand, expanding actuators, for which the zipping of the electrodes translates an extension of the shell similarly to DEA. The main idea behind every design is to come up with a practical way to easily zip the electrodes. This allows for lower operating voltages which is a key factor for these actuators.

As stated before, these actuators have a wide range of applications. Figure 2.3b for example, shows a high-speed application of Peano-HASEL used to lift a table tennis ball into the air. More classical application can also be considered such as in Fig. 2.3c where HASEL actuators are used for pick and place. That last example in particular illustrates the interest of soft actuators as the object to lift (a strawberry) is fragile. Therefore, it requires a soft gripper able to handle its compliance.

Moreover, these actuators present a self-healing feature making them interesting to use when replacement of broken pieces is not possible. This self-healing capability is depicted in Fig. 2.3a. After a dielectric breakdown event, the fluid redistributes itself and regains its insulating state.

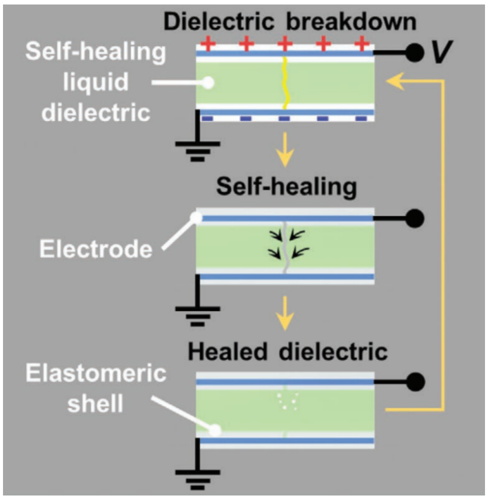

(a) HASEL self-healing property

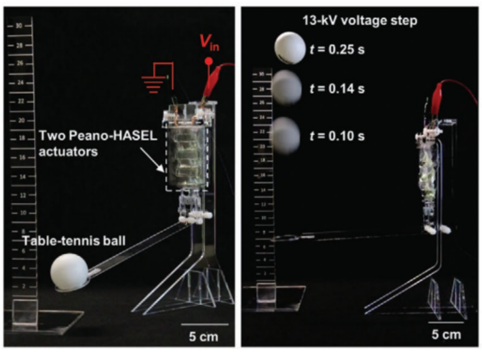

(b) High-speed actuation to lift a table tennis ball in the air

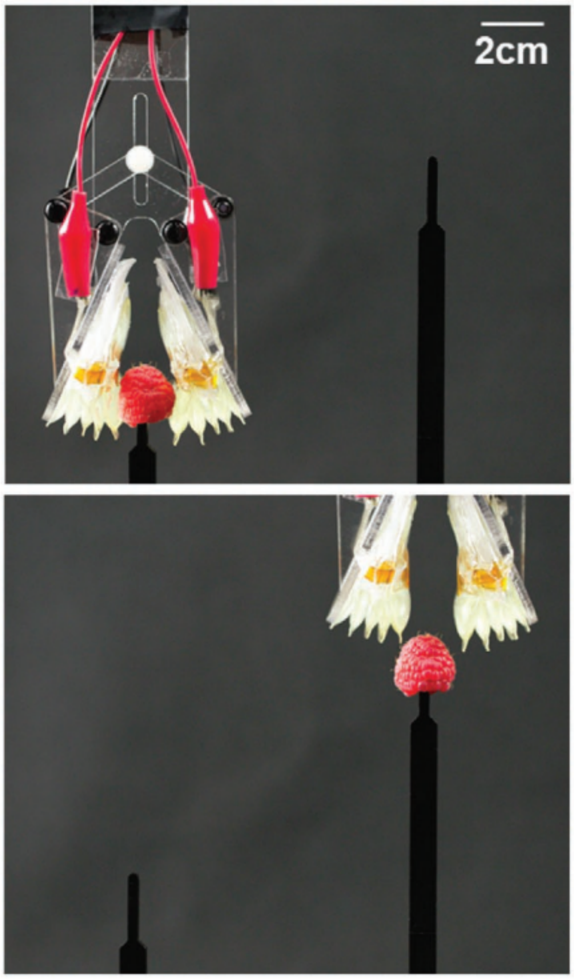

(c) Pick and place application

Figure 2.3: HASEL applications and properties[25]

2.3.1 Donut-shaped HASELs

Fig. 2.4 shows two configurations of donut-shape HASEL. The pouch is a disk with the electrodes located at the center. When a voltage is applied, the dielectric fluid is pushed away from the center as the electrodes zip together. The fully strained pouch takes a torus-like shape. Depending on the radius r of these electrodes, the actuator can either achieve high force but low strain (small r) or low force and high strain (large r)[25] The dimple configuration differs from the quadrant configuration by its number of electrodes. For the quadrant, there are eight electrodes forming four smaller pouches whereas for the dimple there are only two giving a single pouch.

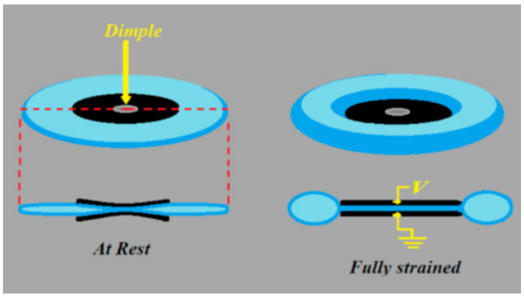

(a) donut HASEL dimple configuration

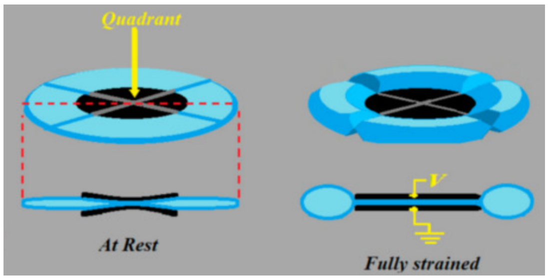

(b) donut HASEL quadrant configuration

Figure 2.4: HASEL donut geometry [25]

2.3.2 Planar HASELs

Planar HASEL is the most common form of HASEL actuators. They are made of two electrode plates squeezing a pouch of rectangular shape in the middle. The pouch is made of an elastomeric shell and filled with dielectric liquid. The electrodes cover a large portion of the pouch such that when a voltage is applied, a decrease in thickness and an increase in area can be observed similarly to DEAs. However, since the pouch contains a liquid instead of multiple elastomeric layers, the stiffness of planar HASEL is lower than the one produced by DEAs (considering the same dimensions and the same materials). It follows that planar HASELs are able to achieve higher actuation strains than DEAs for the same voltage. This has been highlighted by Acome et al. in [1]. They based their planar HASEL actuator design on a laterally constrained DEAs described in [17]. They were able to demonstrate a strain of 79% for a tensile load of 2.5 N when a voltage of 22.5 kV was applied. Fig. 2.5b shows their results.

2.3.3 Peano-HASELs

Peano-HASEL stand out from other kinds of actuators by their ability to contract without needing prestretch rigid frames or stacked configurations. They are a combination of contracting Peano-fluidic actuators and the electrostatic principles of elastomeric HASEL[15].

Made from rectangular shells of flexible polymer films, they are filled with a liquid dielectric sealed to form a pouch. Electrodes are then placed on either side and covering a portion of the shell. When a voltage is applied to these electrodes, the electric fields generated cause the electrodes to zip together progressively leading to a displacement of

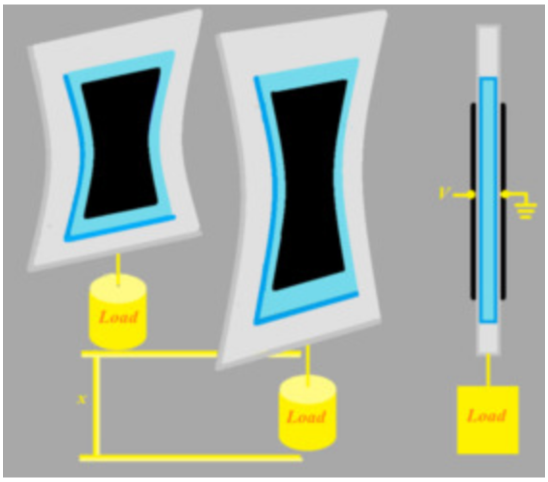

(a) Planar HASEL geometry

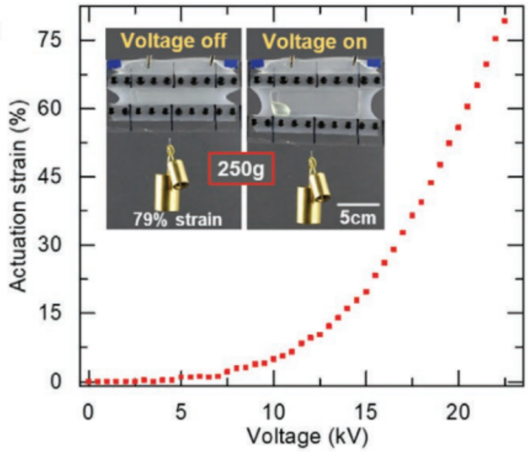

(b) Evolution of Planar HASEL actuation with respect to the voltage applied under a constant 2.5 N load

Figure 2.5: Planar HASEL [25]

the liquid dielectric. Due to the inextensibility of the pouch, the hydrostatic pressure inside the shell increases causing a linear contraction.

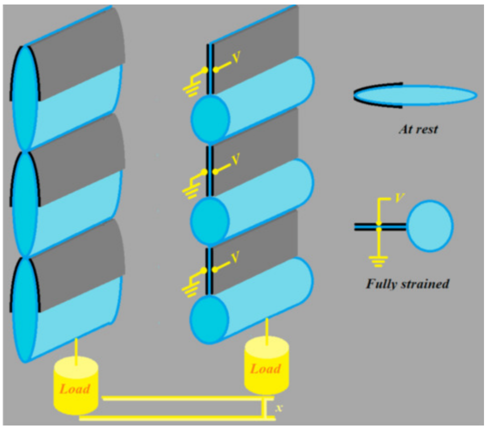

(a) Peano-HASEL geometry [25]

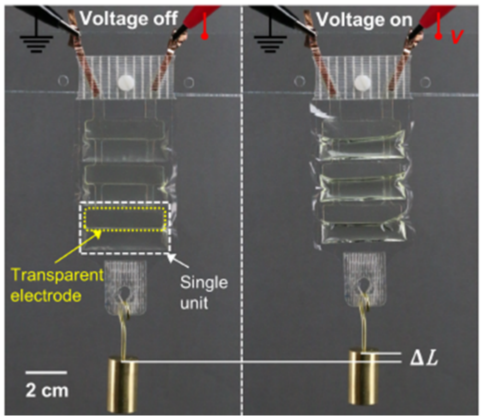

(b) Peano-HASEL contraction to lift a 200 g weight

Figure 2.6: Peano-HASEL actuator

2.4 Analytical model

In 2018, Kellaris et al. developed an analytical model to describe Peano-HASEL actuators and analyze their performance [16].

2.4.1 Geometry of the pouch and stroke definition

Regarding the geometry of the Peano-HASEL, they considered a cross section in Fig. 2.7. The geometry is described by the following parameters: h the height of the pouch, t its thickness, w its width (not visible on the scheme), L_p its arc length, L_e the arc length of the part of the pouch filled with electrodes and α the opening angle of the pouch. Initially, this angle is set to α_0 which corresponds to the initial angle of the pouch once it has been filled with the dielectric liquid and no voltage is applied. Equivalently, r_0 is defined as the initial radius for which the arc length is equal to L_p. Following this, r_0 is equal to:

$$r_0 = \frac{L_p}{2\alpha_0} \tag{2.1}$$

and the area of the sector can be computed as:

$$A_s = \alpha_0 (r_0)^2 = \frac{L_p^2}{4\alpha_0} \tag{2.2}$$

The cross-section area A is obtained by subtracting the area of the triangle from the area of the sector as shown in Fig. 2.8 adapted from [16]. Considering the surface of the green triangle A_t as:

$$A_t = \frac{Ch}{2} = \frac{r_0 \ \cos(\alpha_0) \ h}{2} \tag{2.3}$$

Using the fact that h is equal to:

$$h = 2 \ r_0 \ \sin(\alpha_0) = L_p \left(\frac{\sin(\alpha_0)}{\alpha_0} \right) \tag{2.4}$$

The final formula for the cross section area A can be obtained:

$$A = 2(A_s - A_t) = \frac{1}{2} L_p^2 \left(\frac{\alpha_0 - \sin(\alpha_0) \ \cos(\alpha_0)}{\alpha_0^2} \right) \tag{2.5}$$

Using this last result, the evolution of L_p and L_e according to the pouch deformation can now be derived. Assuming A remains constant during the deformation the following development can be made:

$$l_p(\alpha) = \sqrt{\frac{2A\alpha^2}{\alpha - \sin(\alpha)\cos(\alpha)}} \tag{2.6a}$$

$$l_e(\alpha) = L_p - l_p(\alpha) \tag{2.6b}$$

where $l_p(\alpha)$ and $l_e(\alpha)$ denote the same quantities as L_p and L_e but evolving with respect to α as the pouch is being deformed. Finally, the stroke $x(\alpha)$ visible on parts B. and C. in Fig. 2.7 can be written as:

$$x(\alpha) = h - \left(l_p(\alpha) \frac{\sin(\alpha)}{\alpha} + l_e(\alpha) \right) \tag{2.7}$$

2.4.2 Evolution of the angle α during deformation

The main geometrical variable to take into account is the angle α corresponding to the opening angle of the pouch. Initially, as the pouch is filled with a dielectric liquid and no voltage is applied, the angle α is equal to α_0 as described before. However, as it can be seen in Fig. 2.7, it reaches a critical value α_f once the maximum stroke, written $x(\alpha_f)$ occurs. This happens either when:

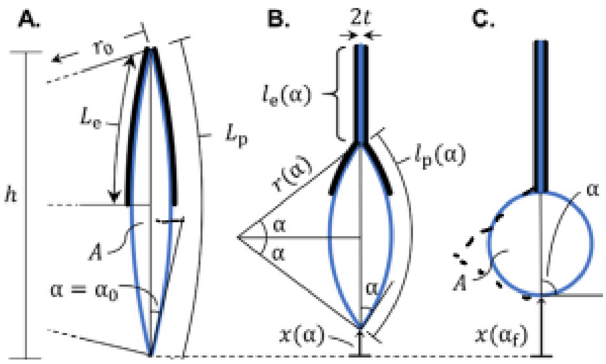

Figure 2.7: Cross-sectional view of a Peano-HASEL: A. Initial configuration: the muscle is at rest and no tension is applied. B. Intermediate configuration: the electrodes are partially closed, and the pouch is deformed by an angle α. C. Final configuration: the electrodes are joined, the deformation is at its maximum, and the angle $\alpha = 90$ °[16]

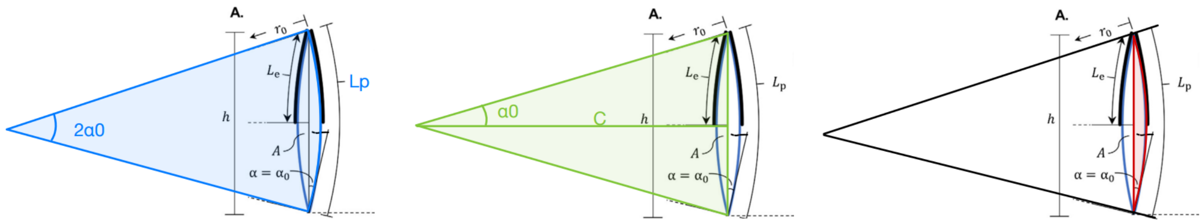

Figure 2.8: Blue: sector area defined by the radius r_0 and the angle $2\alpha_0$. Green: triangle area defined by the basis h and the height C. Red: area obtained after subtracting the green one from the blue one.

1. The electrodes are fully zipped (C) meaning $l_e(\alpha) = L_e$ with L_e the total length of the electrodes covering the pouch.

2. The fluid-filled region takes a circular cross-section ($\alpha = \frac{\pi}{2}$). In that case, a maximum zipping length l_{max} is defined by substituting the value of $\alpha = \frac{\pi}{2}$ in Eq. 2.6b : $l_{max} = L_p - \sqrt{\pi A}$. The angle α_f occurring at the maximum stroke is then found by solving the following equation:

$$L_e = L_p - l_p(\alpha_f) \tag{2.8}$$

This variable also links the stroke and the force developed by the actuator as described in [16].

2.4.3 Development of the closing force

To obtain the closing force of the actuator Kellaris et al. first derived the total free energy of the system which includes the electrical energy stored in the actuator, the contribution from an external force F interacting with the actuator and the electrical energy exchanged with a battery of constant voltage V. The mechanical energy stored in the actuator has been neglected. By defining the capacitance of the zipped region as :

$$C(\alpha) = \frac{\epsilon_r \epsilon_0 w}{2t} l_e(\alpha) \tag{2.9}$$

where ϵ_r is the relative permittivity of the shell and ϵ_0 the permittivity of the free space. The electrical free energy U_e is then given by:

$$U_e = \frac{1}{2}\frac{Q^2}{C(\alpha)} \tag{2.10}$$

with Q symbolizing the charges deposited on the capacitor electrodes. The free energy of the battery decreases by $-QV$ when the charges Q flow from the battery to the actuator. Finally, the work of the external force F over a contraction $x(\alpha)$ is written as $F \cdot x(\alpha)$. The total free energy of the system U_t is thus equal to:

$$U_t(\alpha, Q) = \frac{1}{2}\frac{Q^2}{C(\alpha)} - QV + Fx(\alpha) \tag{2.11}$$

Using $Q = CV$, the expression can be simplified to:

$$U_t(\alpha) = Fx(\alpha) - \frac{1}{2}C(\alpha)V^2 \tag{2.12}$$

By minimizing with respect to α and solving the equation for the applied force F:

$$F = \frac{w}{4t}\frac{\cos(\alpha)}{1-\cos(\alpha)}\epsilon_0\epsilon_r V^2 \tag{2.13}$$

with V the voltage applied to the electrodes, w the width of the pouch and t its thickness. From this equation they observed the following behavior:

1. F is independent of pouch length L_p
2. F scales linearly with w
3. F is inversely proportional to t for a given electric field E
4. F depends on a Maxwell stress term ϵ_0 ϵ_r V^2

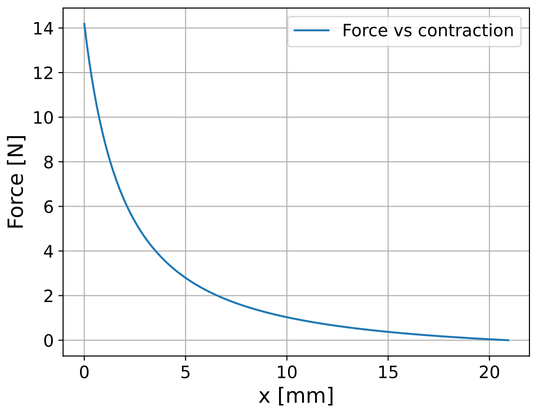

Figure 2.9: Force-displacement $F - x$ characteristic of the HASEL actuator

2.4.4 Analysis of the force-displacement $F - x$ characteristic

Figure 2.9 depicts the force-displacement characteristic of the Peano-HASEL actuator. Several observations can be made. First, the blocking force F_b of the actuator, corresponding to the maximum force the actuator can generate without any displacement ($x = 0$) is reached at $\alpha = \alpha_0$. As stated in Eq. 2.7, at this angle the displacement is equal to 0. Secondly, the slope of the characteristic, corresponding to the stiffness of the actuator, is decreasing and nonlinear. This behavior distinguishes HASELs from their biological inspiration where the phenomenon is reversed.

2.4.5 Scaling properties of Peano HASEL actuators

Kellaris et al. identified two fundamental properties regarding Peano-HASEL actuators:

- As illustrated in Fig. 2.10a, a single pouch of arc length L_p and mass $m = m_{\text{act}}$ can be divided into n sub-pouches of arc length $\frac{L_p}{n}$ and mass $\frac{m}{n^2}$. This geometric scaling does not affect the $F - x$ characteristic of the actuator meaning the output force F and displacement Δx produced remain unchanged. The main benefit of this observation is that the mass of the actuator m_{act} is divided by n the number of sub-pouches. The practical drawback is the need to connect these pouches together sacrificing a portion of the contraction Δx to that end.

- As shown in Fig. 2.10b, Peano-HASEL can be put in parallel to scale up the total output force F of the actuator. In this configuration, the individual pouch length L_p can be reduced inherently decreasing the radius R of the fluid filled region when the actuator is in its fully contracted state ($\alpha_f = \frac{\pi}{2}$). Neglecting the film thickness t, this smaller radius R allows for an increasing stacking density of the pouches. This stacking density scales inversely with the arc length L_p and, by keeping the cross section A constant, it scales linearly with the output force F.

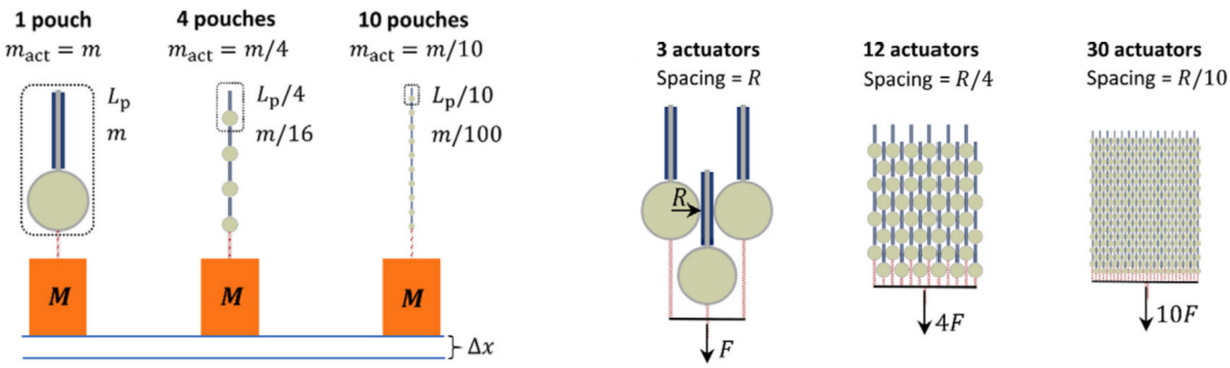

(a) Peano-HASEL series configuration (b) Peano-HASEL parallel configuration

Figure 2.10: Peano-HASEL scaling properties adapted from [16]

Chapter 3

Problem statement

This chapter first presents the antagonistic application considered in this master thesis. Next, it highlights the differences between the bio-inspired model and the biological one. Then, it introduces the specifications of the application based on muscle properties. Finally, it expresses the need for dimensioning methods and the physical limitations of this application.

3.1 Description of the antagonistic Application

As described previously, the purpose of this master thesis is to propose a method to find the best geometrical parameters of an HASEL artificial muscle (L_p, α_0, w, t) for a given antagonistic application. In our case, we considered an antagonistic application characterized by the presence of an agonist muscle (often also called prime mover), causing the motion, and an antagonist muscle that opposes the movement of the agonist. There are numerous examples for this configuration in the musculoskeletal system: biceps and triceps for the elbow, quadriceps and hamstrings for the knee, etc.[9]

This configuration allows for the control of the torque τ, the angular position $\Delta\theta$ and the angular stiffness R at the joint. The latter is controlled through the co-contraction of the agonist and antagonist muscles. In particular, Hogan has shown in his work that this stiffness R can be modulated to perform adaptive control of mechanical impedance while the angular position $\Delta\theta$ and torque τ can be decoupled and controlled independently [13].

The configuration of our application can be seen in Fig. 3.1. Two HASEL actuators (denoted by numbers (1) and (2) on the schematic) are linked to a pulley of radius r (3) fixed to the base. An arm (4) is attached to the pulley to measure the relative angular motion $\Delta\theta$ and the angular stiffness R .

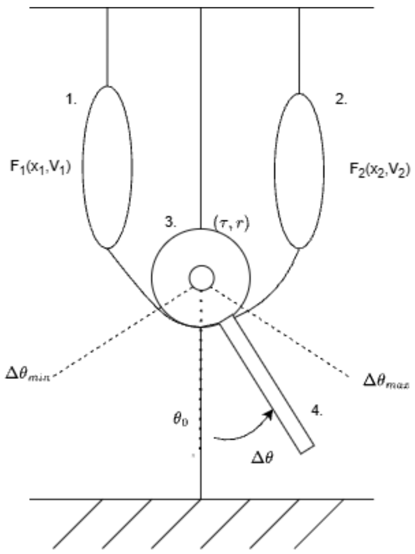

Figure 3.1: Antagonistic configuration: (1) and (2) HASEL actuators. (3) pulley of radius r representing the joint where a torque τ is produced. (4) Arm

3.2 Differences with the bio-inspiration

The objective with this application is not to replicate the biological structure of muscles but rather to mimic their behavior. To that end, we have considered several simplifications to our mechanical model with respect to its bio-inspiration.

First, the system depicted in Fig. 3.1 focuses only on one set of motions. Taking the example of the elbow, it only reproduces the flexion-extension movement of this joint. Pronation-supination, adduction-abduction and other types of more complex motions are not being considered here. This choice facilitates the analysis of the system (described in chapter 5) and truly isolates one set of specifications.

In line with the first point, by only considering one kind of movement (flexion-extension) we can simplify the system to one set of muscles and not take into consideration the human body redundancy. This redundancy implies that the human body is over-actuated, meaning several groups of muscles are used to perform the same kind of motion.

Referring back to the elbow example in Fig. 3.2a, the brachialis and brachioradialis muscles are called synergists because they help the biceps perform the flexion movement. Specifically, while the brachioradialis only acts as a stabilizer, to guide the motion, the brachialis plays a more decisive role. It has been demonstrated that it acts as the prime agonist muscle during the flexion motion instead of the biceps [9]. However, for our application, we have considered the biceps and triceps as they are better positioned and benefit from a greater lever arm.

Another simplification made is to consider the joint as a pulley of constant radius r while in reality, biological joints are complex surfaces with varying lever arms depending on the motion performed. This assumption is based on the work of Aliman et al. who demonstrated that biological joints can be replicated using several pulley arrangements [2]. Furthermore, this constant radius r, coupled with two muscles of the same length and a strategic positioning of the reference angle θ_0, allows for a symmetrical range of motion, whereas biological systems often do not as depicted in Fig. 3.2b.

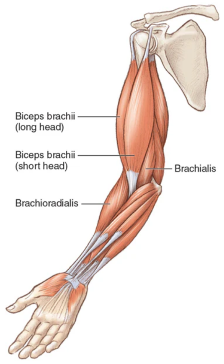

(a) Main muscles of the elbow for the flexion-extension movement: [5]

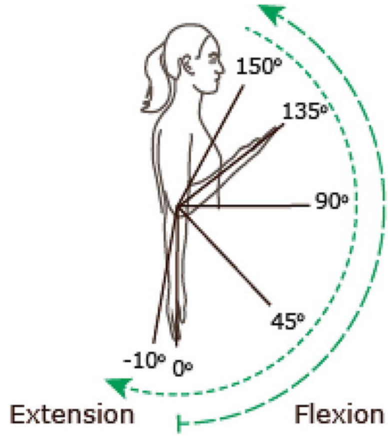

(b) Range of motion of the elbow [22]

Figure 3.2: Description of the elbow joint

3.3 Specifications of the application

Having described the mechanical model of the application and how it differs from the biological one, we must now define its specifications. Each HASEL actuators used in the system is able to produce a force F and a displacement x following the characteristic in Fig.2.9. At the same time, these muscles also produce a torque τ at the joint:

$$\tau = r(F_2 - F_1) \tag{3.1}$$

This equation expresses how the forces F_2 and F_1 of the HASEL actuators affect the torque τ considering a constant radius r. Similar to biological joints, the joint must be able to rotate within a certain angular range delimited by $\Delta\theta_{\text{min}} = -\Delta\theta_{\text{max}}$ and $\Delta\theta_{\text{max}}$ the minimum and maximum relative angles with respect to a reference angular position θ_0. At this reference angle, both muscles have the same length. A relative displacement Δx is associated with a relative angle $\Delta\theta$:

$$r\Delta\theta = \Delta x \tag{3.2}$$

As both muscles are linked to the pulley, if one contracts by Δx the other extends by Δx just like in the bio-inspired system. However, an HASEL actuator cannot extend beyond its height h without tearing the pouch apart leading to complete failure of the system. Therefore, we need to pre-stretch these muscles from a certain initial length denoted x_{init} in Fig. 3.4b. The choice of x_{init} will be discussed further in Section 3.4. Taking the pre-stretch into account we can use Eq. 3.2 to define x_1 and x_2 :

$$x_1 = x_{\text{init}} - \Delta x \tag{3.3}$$
$$x_2 = x_{\text{init}} + \Delta x \tag{3.4}$$

Apart from the torque and the angular position, we are also interested in studying the stiffness produced at the joint. This stiffness, denoted R, is obtained by taking the derivative of τ with respect to θ:

$$
\begin{aligned}
R &= \frac{\mathrm{d}\tau}{\mathrm{d}\theta} \\
&= r\left[\frac{\mathrm{d}F_2}{\mathrm{d}\theta} - \frac{\mathrm{d}F_1}{\mathrm{d}\theta}\right] \\
&= r\left[\frac{\mathrm{d}F_2}{\mathrm{d}\alpha_2}\frac{\mathrm{d}\alpha_2}{\mathrm{d}x_2}\frac{\mathrm{d}x_2}{\mathrm{d}\theta} - \frac{\mathrm{d}F_1}{\mathrm{d}\alpha_1}\frac{\mathrm{d}\alpha_1}{\mathrm{d}x_1}\frac{\mathrm{d}x_1}{\mathrm{d}\theta}\right] \\
&= r^2\left[\frac{\mathrm{d}F_2}{\mathrm{d}\alpha_2}\frac{\mathrm{d}\alpha_2}{\mathrm{d}x_2} + \frac{\mathrm{d}F_1}{\mathrm{d}\alpha_1}\frac{\mathrm{d}\alpha_1}{\mathrm{d}x_1}\right]
\end{aligned} \tag{3.5}
$$

where the derivative of the force F with respect to the opening angle α is :

$$
\frac{\mathrm{d}F}{\mathrm{d}\alpha} = -\frac{w}{4t}\frac{\sin(\alpha)}{(1-\cos(\alpha))^2}\epsilon_0\epsilon_r V^2 \tag{3.6}
$$

and the contraction term is obtained through:

$$
\left(\frac{\mathrm{d}\alpha}{\mathrm{d}x}\right) = \left(\frac{\mathrm{d}x}{\mathrm{d}\alpha}\right)^{-1} = \left(-\left[\left(\frac{\mathrm{d}}{\mathrm{d}\alpha}(l_p(\alpha))\right)\left(\frac{\sin(\alpha)}{\alpha} - 1\right) + l_p(\alpha)\left(\frac{\cos(\alpha)\ \alpha - \sin(\alpha)}{\alpha^2}\right)\right]\right)^{-1} \tag{3.7}
$$

with the arc length $l_p(\alpha)$ equal to:

$$
l_p(\alpha) = L_p\frac{\alpha}{\alpha_0}\sqrt{\frac{\alpha_0 - \sin(\alpha_0)\cos(\alpha_0)}{\alpha - \sin(\alpha)\cos(\alpha)}} \tag{3.8}
$$

Eq.3.7 in particular is analytically complex to evaluate. We thus considered a numerical evaluation, using a second-order centered difference to ensure numerical stability.

Eq. 3.5 can also be rewritten to express the linear stiffness of each artificial muscle:

$$
R = r^2[K_2 + K_1] \tag{3.9}
$$

highlighting the fact that the angular stiffness at the joint is the sum of the linear stiffnesses (K_1, K_2) of the artificial muscles corresponding to the slopes of their $F-x$ characteristics.

Examining Eqs. 3.6 , 3.7 we can see that they mainly depend on four geometric parameters: L_p, α_0, t and w. While some of these geometric parameters scale linearly, the way they interact with each other does not provide a clear conclusion on an optimal geometry that satisfies given specifications. In particular, α_0 also acts as a lower boundary for α making the analysis of these equations even more complex. Therefore, we must develop a dimensioning methodology to design HASEL artificial muscles such that the joint can achieve a certain torque τ while covering specific ranges of stiffness R and angle $[-\Delta\theta_{\max}, \Delta\theta_{\max}]$.

3.4 Physical limits of the application

The system described above suffers from several limitations due to its geometry and materials used for its fabrication. Fig. 3.4a shows the maximal contraction, denoted

$x_{\text{max rot}}$, the system is able to produce. This value is reached for a relative angle $\Delta\theta$ equal to $\Delta\theta$max. As stated in the previous section, beyond this contraction the first pouch (1) would be overstretched and could break, leading to a global failure of the system. To avoid this, we must impose the following constraint on the displacement:

$$x_f \geq 2\ x_{\text{max rot}} \tag{3.10}$$

where x_f corresponds to $x(\alpha_f = \frac{\pi}{2})$ the displacement for which the pouch adopts a circular shape. For the sake of simplicity, we assume the hypothesis of optimum-filling to still hold here, meaning the pouch is fully deformed ($\alpha_f = \frac{\pi}{2}$) when it is fully zipped.

x_{init},the pre-stretch described in the last section, is expressed as a percentage of this x_f. Figs. 3.3a , 3.3b illustrate two choices of x_{init}: $\frac{1}{2}\ x_f$ and $\frac{1}{4}\ x_f$. Taking half the value of the maximum contraction ensures that we maximize the angular range we can cover but it limits the stiffness produced as we are working in a flatter area of the characteristic. Taking 25 % of x_f allows us to gain better torque and stiffness as we are positioned on a steeper part of the characteristic. The drawback is that the angular range is reduced as the stroke of the actuator elongating will be shorter. More specifically, the actuator will elongate until it reaches the physical limit $x = 0$. If the system goes beyond this limit, the actuator in extension could break as mentioned before. Considering the angular range of our specifications, we chose to set $x_{\text{init}} = \frac{1}{2}\ x_f$.

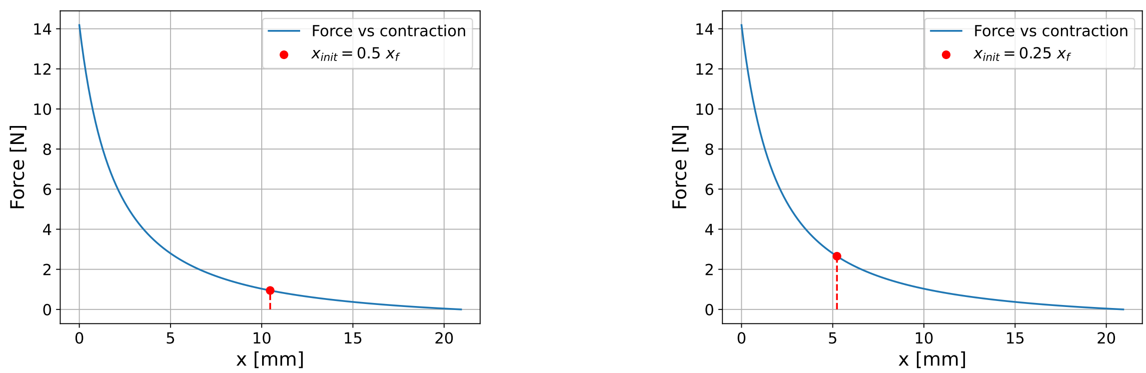

(a) $x_{\text{init}} = \frac{1}{2}x_f$

(b) $x_{\text{init}} = \frac{1}{4}x_f$

Figure 3.3: Several x_{init} values illustrated on the $F - x$ characteristic of HASEL muscle

Another physical limit of the system that we need to address, is the voltage range. Indeed, while HASELs muscles require a significant voltage to be able to contract ($\sim$ kV) previous work has proved that around 8 kV electric arcs begin to form inside the plastic pouch leading to its degradation [28] (given a certain type of dielectric liquid and plastic material). Therefore, we must constrain the search space to work within the following voltage range: $V \in [V_{\text{min}}, V_{\text{max}}]$ with $V_{\text{min}} = 500$ V and $V_{max} = 7$ kV. The lower limit has been fixed to an arbitrary value of 500 V to avoid having a fully relaxed muscle while the upper limit is fixed to 7 kV to maintain a safety margin with respect to the breakdown value of 8 kV.

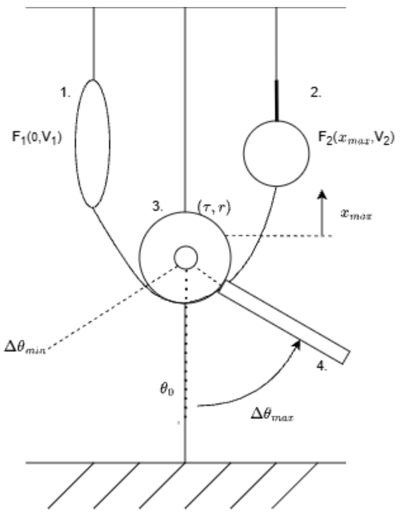

(a) Maximal displacement of the configuration around the operating point defined by $(\tau, \Delta\theta = \Delta\theta_{\max})$

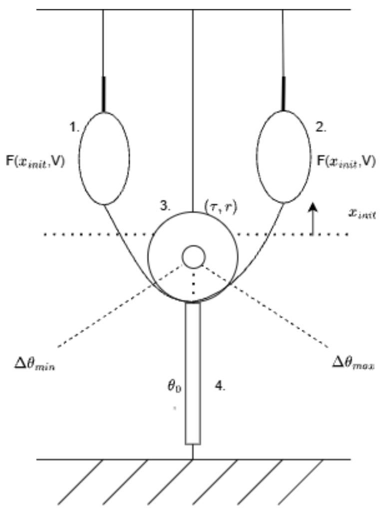

(b) Initial state of the configuration around the operating point defined by $(\tau, \Delta\theta = 0)$ where a pre-stretch x_{init} is applied to both muscles

Figure 3.4: Boundary conditions of the antagonistic application

Chapter 4

Methodology

In this chapter, we describe the methods developed to find the optimal geometry ruled by four geometrical parameters: L_p, α_0, w and t in order to meet the constraints and the specifications introduced in Chapter 3. We first present the common structure both algorithms use to compute the stiffness. Then we describe the GS algorithm, an exhaustive approach that searches for all solutions within a certain search space. Afterwards, we present the CMOPSO[18], an optimization algorithm based on classical Particle Swarm Optimization (PSO) [27] and the evolutionary Non-dominated Sorting Genetic Algorithm II (NSGA-II) [8]. For both the grid search and CMOPSO, we shall motivate their use, explain their global principles and demonstrate how they can be applied to this dimensioning problem.

4.1 Search space

The search space is the four-dimensional space $\mathbb{R}^4$ described by $L_{p\text{ range}}$, $\alpha_{0\text{ range}}$, w_{range} and t_{range} which are bound as follows;

1. $L_{p\text{ range}} = [L_{p\text{ min}}, L_{p\text{ max}}]$
2. $\alpha_{0\text{ range}}$ =[$\alpha_{0\text{ min}}$, $\alpha_{0textmax}$]
3. $w_{\text{range}} = [w_{\text{min}}, w_{\text{max}}\ ]$
4. $t_{\text{range}} = [t_{\text{min}}, t_{\text{max}}]$

Both algorithms work within the same search space. The only difference lies in the fact that GS is a discrete algorithm while CMOPSO is continuous. Therefore, GS requires a step size for each dimension. The values of these steps will be discussed in Chapter 5.

4.2 Constraints

Both algorithms implement the constraints described in Section 3.4. Specifically, the voltages V_1 and V_2 actuating the muscles must lie within a specified range $[V_{\text{min}}, V_{\text{max}}]$. Furthermore, the free stroke x_f must be at least twice the displacement associated with the maximal rotation $\Delta\theta_{\text{max}}$ to prevent the antagonistic muscle from reaching its physical limit during joint rotation. Finally, the angular stiffness R produced at the joint must encompass the target stiffness range described in the specifications. Additionally, the search space boundaries described in the previous section act as direct geometrical constraints on L_p,α_0,t and w.

4.3 Stiffness computation loop

The following pseudo-algorithm describes a common part shared by both algorithms: the stiffness computation loop. It implements the specifications and limitations described in the previous chapter for each candidate $c = (L_p, \alpha_0, w, t)$ or particle $p = (L_p, \alpha_0, w, t)$ considered either by GS or CMOPSO :

Algorithm 1: Stiffness computation

```
Δx ← rΔθ
F₂ ← F₁ + τ/r
for i = 1 to N do
    Compute pouch height h using Eq. 2.4
    Compute cross-sectional area A using Eq. 2.5
    Compute x_f and deduce the pre-contraction x_init using Eq. 2.7 assuming
      optimum filling
    x₁ ← x_init − Δx
    x₂ ← x_init + Δx
    Find α₁ corresponding to x₁ by solving Eq. 2.7
    Find α₂ corresponding to x₂ by solving Eq. 2.7
    Compute voltage range V₁ using F₁, α₁ in Eq. 2.13
    Compute voltage range V₂ using F₂, α₂ in Eq. 2.13
    Compute ∂F₁/∂α₁ and ∂F₂/∂α₂ using Eq. 3.6
    Compute dα₁/dx₁ and dα₂/dx₂ using Eq. 3.7
    Compute stiffness R using Eq. 3.5
end
```

4.4 Methods implementation

4.4.1 Grid search implementation

The principle behind the grid search algorithm is to find all possible solutions within the search space. A solution is a candidate $c = (L_p, \alpha_0, w, t)$ that satisfies the desired range of stiffness presented in Section 3.3 while respecting the constraints on voltage and geometry addressed in Section3.4. The stiffness and voltages are computed within the stiffness loop described in Algorithm 1. To verify whether these constraints are satisfied, we implemented two filters named respectively "Geometric filter" and "Stiffness and voltage filter" which can be seen on the schematic of the algorithm depicted in Fig. 4.1. In addition, to extract the best results with respect to certain criteria, a Pareto selection filter was also implemented. This last filter is optional and is treated not as a part of the algorithm but rather as a post-processing step to analyze the results.

Initialization

First, the algorithm initializes the boundaries of each variable L_p, α_0, w, t as well as the specifications S regrouping the torque τ, the radius r, the angular range of motion $[-\Delta\theta_{\max}, \Delta\theta_{\max}]$, the angle $\Delta\theta$ and the desired stiffness range R. Conveniently, the specifications S also contain the constraints on the voltage range $[V_{\min}, V_{\max}]$ as well as some physical constants like ϵ_r and ϵ_0 the relative and vacuum permittivities. Additionally, it also contains the force range F_1 (or F_2) initialized at the beginning of the Algorithm 1. This force range is assumed to be known (and found experimentally) as it is necessary to find the voltage ranges V_1 and V_2 using Eq. 2.13. The force range corresponding to the other artificial muscle (here F_2) is found using Eq. 3.1.

Geometric filter

The Geometric filter takes as input the full search space $\mathbb{R}^4$ and returns as output a subspace restricting L_p and α_0 . Its main purpose is to ensure that the candidate c verifies the geometric conditions on x_f described by Eq. 3.10.

Stiffness and voltage filter

This filter takes as input all the candidates c that passed the geometric one. Then, using the stiffness R and voltages range V_1, V_2 computed in algorithm 1 for each candidate, it determines if the corresponding candidates c are part of the solution space which contains all possible configurations.

Pareto filter

This filter evaluates each solution to select those that minimize certain criteria like the mass or a specific dimension of the artificial muscle. This filter is applied as a post-processing step of the GS algorithm.

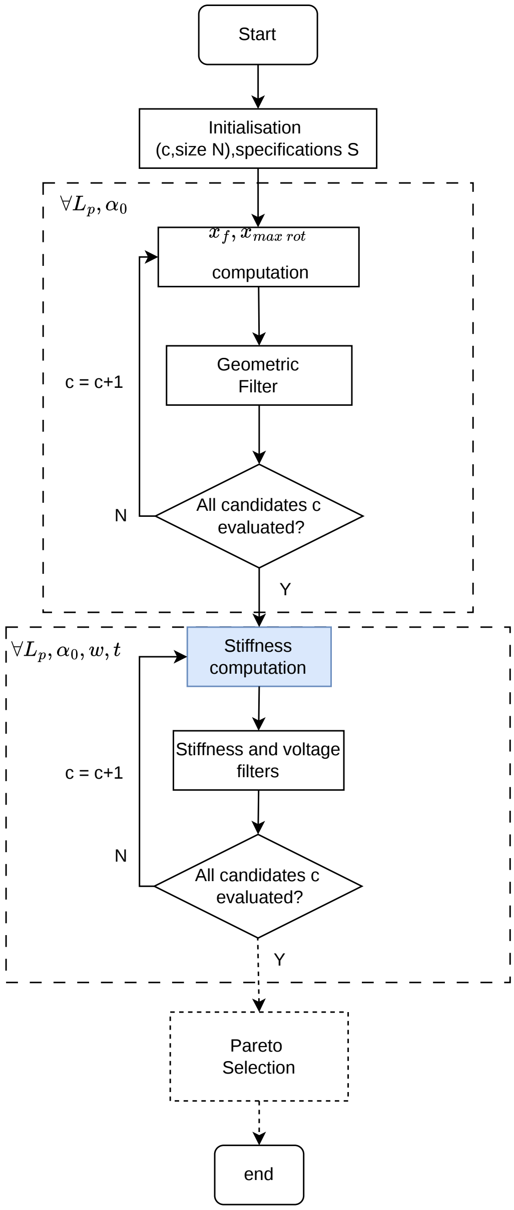

Figure 4.1: Grid search algorithm overview. Blue: the stiffness computation block detailed by algorithm 1

4.4.2 Competitive Multi-Objective Particle Swarm Optimization (CMOPSO) implementation

While offering an exhaustive solution to our problem, the grid search algorithm suffers from high computational cost as soon as the search space becomes too large. Another interesting approach we have considered to tackle this problem is an optimization approach. It uses a heuristic strategy to solve the problem aiming to find a global optimum.

The algorithm is based on the idea of a trade off between exploring the search space and exploiting the results from the exploration. It consists of a classical Particle Swarm Optimization PSO algorithm with a population of particles exploring a search space. Here, each particle p is defined by a combination of (L_p, α_0, w, t) and by the following objective functions:

$$
\begin{aligned}
\min \quad F = \min \quad & [f_h, f_w, f_m]^T \\
s.t. : & V_{\min} \leq V_1, V_2 \leq V_{\max} \\
& R_{\min} \leq R_{\min \text{ des}} \\
& R_{\max} \geq R_{\max \text{ des}} \\
& x_f \geq 2 \, r \Delta\theta_{\max}
\end{aligned}
\tag{4.1}
$$

where the vector of objective functions F regroups the following three objective functions:

$$
\begin{cases}
f_h = h \\
f_w = w \\
f_m = m_{\text{tot}}
\end{cases}
$$

The objective vector tends to minimize the height h the width w and the total mass m_{tot} of the actuator while respecting the constraints described in Section 3.4. The constraints are the same as for the grid search. The difference between the two implementations lies in the way these constraints are interpreted. CMOPSO will associate a high cost to these constraints so that the solver will avoid transgressing them (as it wants to minimize the objective function) whereas for GS, the constraints are imposed as hard *if - else* conditions. The total mass of the actuator is computed as:

$$
\begin{aligned}
m_{\text{plastic}} &= 2 \, t \, w \, h \, \rho_p \\
m_{\text{oil}} &= A \, w \, \rho_o \\
m_{\text{tot}} &= m_{\text{plastic}} + m_{\text{oil}}
\end{aligned}
\tag{4.2}
$$

where $\rho_p = 910[\frac{kg}{m^3}]$ and $\rho_o = 930[\frac{kg}{m^3}]$ are the densities of the plastic pouch and of the dielectric liquid (here oil). While those objectives are linked and influence each other, the algorithm aims to find a set of solutions for which constraints are respected and objectives are minimized.

Contrary to simple PSO, CMOPSO uses a vector of objective functions for optimization. It also differs in the way it updates the position of the particles. For PSO, the particles' positions are updated using the following equation:

$$x_i^{t+1} = x_i^t + v_i^{t+1} \tag{4.3}$$

where:

$$v_i^{t+1} = \omega \; v_i^t + c_1 \; r_1 \; (p_i^t - x_i^t) + c_2 \; r_2 \; (g^t - x_i^t) \tag{4.4}$$

with:

- $\omega \; v_i^t$ representing the inertial component of the particle
- $c_1 \; r_1 \; (p_i^t - x_i^t)$ is its cognitive component where p_i^t represents the personal best estimation of the solution made by the i-th particle at time t (denoted x_i^t)

- $c_2\ r_2\ (g^t - x_i^t)$ represents the social component of the particle, which quantifies how much the velocity of the particle is influenced by the global estimate g^t of the entire population.

r_1 and r_2 are random numbers uniformly distributed between 0 and 1 and used to add stochasticity in the algorithm. They ensure that the algorithm is not trapped in a local minimum. They also promote exploration of the search space. Finally, they scale c_1 and c_2, the weights influencing the cognitive and social components, so that the attraction toward the personal and global best p_i^t and g^t is not deterministic. In the literature, those weights are usually fixed to standard values: $\omega = 0.6$, $c_1 = 1.5$, $c_2 = 1.5$ even though more thorough investigations into these weights have been conducted.[21]. Indeed, they can be tuned depending on whether we want to promote exploration ($c_1 > c_2$) or exploitation ($c_2 > c_1$). High values of ω (0.9) tend to favor exploration while low values (0.4) favor exploitation. A common practice is to reduce the value of this inertial weight ω as the number of iterations of the algorithm increases. This approach ensures stable convergence.

In CMOPSO, the update of the particle works the same way except that the population of particles is divided into two sets: the winners forming the Pareto front and the losers. When the velocity is updated, the cognitive component of the losers is replaced by the personal best of the closest winner:

$$v_{l,k}(t+1) = r_1(k,t)v_{l,k}(t) + r_2(k,t)(x_{w,k}(t) - x_{l,k}(t)) + \phi r_3(k,t)(g_k(t) - x_{l,k}(t)) \quad (4.5)$$

where: $r_1(k,t), r_2(k,t)$ and $r_3(k,t)$ are uniformly distributed random numbers between 0 and 1, $x_{l,k}(t)$ and $x_{w,k}(t)$ are the loser and winner particles positions at time t after the kth competition and ϕ is a weight controlling the influence of the global solution $g_k(t)$ representing the mean position of all the particles in the swarm.

The distinction between winners and losers is determined by the competitive mechanism depicted in Fig. 4.2 where a particle P representing a loser from the $k-1$th round must choose between two elite particles a and b to update its position. Since the angle θ_1 between a and P is smaller than θ_2, the angle between b and P, P selects particle a to update its position and a is said to have won the $k-$th round of the competition.

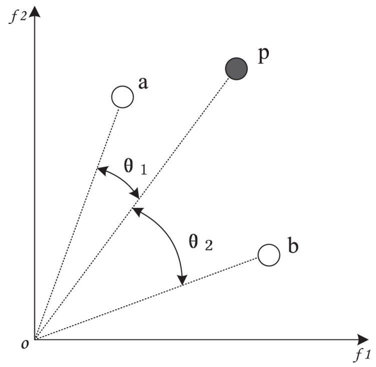

Figure 4.2: Competitive mechanism principle: P the loser from a previous round must choose between two elite particles a and b to update its current position. As $\theta_1 < \theta_2$, a is selected as winner for this round and P updates its position based on a.[18]

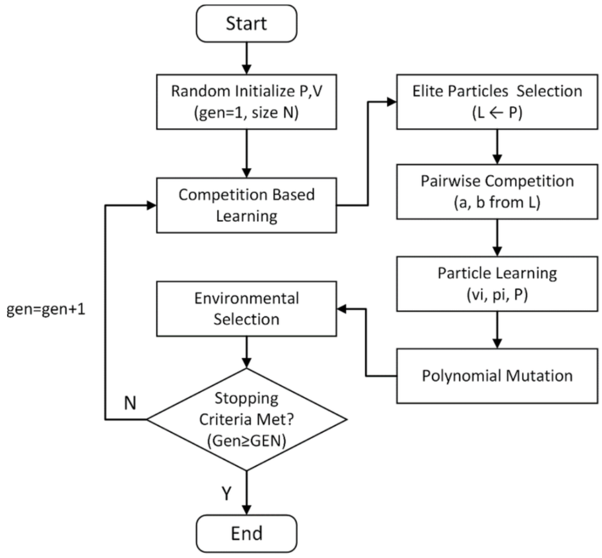

Figure 4.3: Competitive mechanism Multi-Objective Particle Swarm Optimization CMOPSO algorithm. [18]

Another addition made compared to PSO is the polynomial mutation operator applied at the end of each generation and visible on Fig. 4.3. Borrowed from NSGA-II algorithm, it ensures the promotion of exploration at each generation. As in most multiple objective algorithms it also prevents the algorithm from being trapped in local minima [33]. This process is controlled by a mutation rate fixed at 0.5

Fig. 4.3 illustrates the overall workflow of the algorithm. First, it initializes random initial positions p and velocities v for all the swarm. Then, it performs competition-based learning using an evaluation function. For our application, this evaluation function encompasses the stiffness and voltage computation block of Algorithm 1, the computation of the maximal displacement $x_{\text{max rot}}$ and the computation of the total mass of the system m_{tot}. Additionally, this function also evaluates constraint violations.

Chapter 5

Results

This chapter reports the results of the algorithms described above. First, it assigns values for the specifications defined in Chapter 3 considering the example of the elbow. Then, it presents the results of the GS and CMOPSO algorithms before comparing these results. This is followed by a discussion about the nature of these results as well as a study of the force-displacement characteristic ($F - x$) of the HASEL. Afterwards, a sensitivity analysis of the parameters and specifications described in Chapter 4 is conducted. Lastly, the achievable specifications using current HASEL technology are evaluated through an example based on the work of Kellaris [16].

5.1 Specifications values of the elbow

Ideally, the bio-inspired system described in Chapter 3 should be able to replicate the performance of its biological counterpart. Considering the human elbow joint, the range of motion for flexion-extension spans from 150° in flexion to −10° in extension, assuming a reference position where the arm is at rest alongside the body (see Fig. 3.2b). For this specific application, a symmetric angular range going from −80° to 80° is considered.

Regarding the stiffness developed at the joint, the literature provides different values based on the definition of stiffness. In particular, one can distinguish total stiffness from intrinsic stiffness. The intrinsic stiffness is the one related to the tissues and their elastic properties. It is inherently passive, as it does not rely on any active control. In comparison, the total stiffness encompasses the intrinsic stiffness and the stiffness produced by feedback of the neural system. Given this distinction, and since the system described in Fig. 3.1 does not implement any form of feedback, we limit ourselves to an application corresponding to the intrinsic one.

To find that range, we refer to the literature. Shadmehr et al. provide us with a global stiffness range going from 6 to 16 Nm/rad [26]. In another paper, Crevecoeur et al. managed to isolate the intrinsic component of the stiffness for the elbow joint [6]. Considering a lever arm r of 40 mm and a torque τ of 2 Nm, they found a unique value of 1.61 Nm/rad. We can observe that the value found by Crevecoeur for the intrinsic stiffness corresponds to about 10 % of the global stiffness found by Shadmehr. Therefore, we can extend this observation to consider a hypothetical range for the intrinsic stiffness spanning from 0.6 to 1.6 Nm/rad. Finally, we define an operating point requiring a torque $\tau = 2$ Nm and corresponding to the relative angular position $\Delta\theta = 0°$. In particular, this last value was chosen as it lies in the middle of the angular range where, theoretically, the stiffness is at its maximum.

In summary, Table 5.1 gathers the specifications of the application corresponding to a human elbow:

Specifications	
$[R_{\min}, R_{\max}]$	[0.6,1.6] [Nm/rad]
τ	2 [Nm]
$[-\Delta\theta_{\max}, \Delta\theta_{\max}]$	[-80,80] [°]
$\Delta\theta$	0 [°]
r	40[mm]

Table 5.1: Biological specifications of an elbow flexion-extension movement for a given operating point $(\tau, \Delta\theta)$

5.2 Objective space and search space boundaries

The results generated by the algorithms described in Chapter 4 are presented below. To ensure that the results between both methods are comparable, the same objective space was used for both. Thus, the GS results are displayed in the same 3D objective space of the CMOPSO algorithm. As a reminder, this objective space is defined by the height h, the width w and the mass m of the pouch. Moreover, since the search space is common (see Section 4.1), we set the following boundaries (and steps for the GS algorithm):

	Lower boundary	**Upper boundary**	**Step** (GS)
$L_{p\ \text{range}}$ [m]	0.02	4.5	0.02
$\alpha_{0\ \text{range}}$ [°]	5	90	5
$w_{\ \text{range}}$[m]	0.05	8	0.05
$t_{\ \text{range}}$ [µm]	14	50	2

Table 5.2: Search Space boundaries

For $L_{p\ \text{range}}$ and $w_{\ \text{range}}$, the lower boundaries correspond to conventional manufacturable HASEL actuators. The upper boundaries were extended to expand the search space and ensure convergence as the algorithm struggled to find solutions at lower values. Regarding the film thickness t, the values correspond to commercially available dimensions of the material used in the fabrication of the pouch. In this case, Biaxially Oriented Polypropylene (BOPP) was considered for the plastic film, with a relative permittivity $\epsilon_r = 2.2$ and thicknesses t ranging from 14 to 50 µm.

5.3 Grid Search method

Fig. 5.1 shows the results obtained from the GS algorithm. In green are all the feasible solutions found by the algorithm. The red point represents the optimal solution found minimizing all three objectives while still respecting the constraints. A first observation one can make is that the mass of the system increases drastically with respect to h and w. Further explanation regarding this observation is conducted in Section 5.5.

Another observation concerns the orders of magnitude shown in this graph. The solutions for w and h appear to cluster around the upper limits given in Table 5.2. This reflects the difficulty the algorithm encounters in finding a solution that satisfies both the constraints and the specifications.

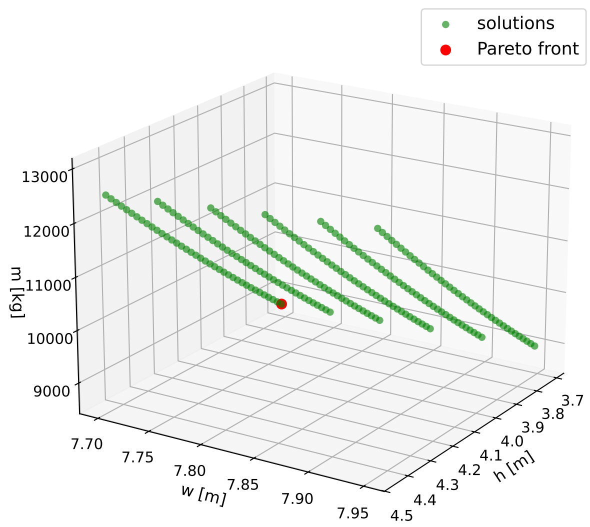

Figure 5.1: Green: grid Search algorithm results. Red: Pareto point extracted with the Pareto selection filter described in Chapter 4

5.4 CMOPSO method

Figures 5.2 and 5.3 illustrate the results obtained with CMOPSO. These results were obtained by running the algorithm 10 times with different initial velocities $v_{i,0}$ and random initial positions $P_{i,0}$ for the particles, in order to account for the stochastic nature of this method. The results cluster around a front. As observed for the GS algorithm, it converges towards the upper bounds of the search space, thus encountering the same difficulties as the GS. With regard to mass, it yields better results, although the resulting dimensions remain physically unfeasible. This improvement is due to the optimizing nature of the algorithm. Moving in a continuous space, the particles are able to reach optimized positions that a fixed-step grid search could not reach. Furthermore, due to numerical tolerances, this algorithm is more likely to accept a solution that slightly violate a constraint threshold (typically by less than 10^{-9}).

An examination of Subfigures 5.3a, 5.3b and 5.3c allows us to draw further conclusions regarding the behavior of the algorithm. The algorithm attempts to minimize the mass m either by adjusting h or by adjusting w, maximizing one to minimize the other. However, the set of solutions tends to cluster around low values of h and corresponding high values of w, rather than the reverse, indicating that the algorithm exhibits a higher sensitivity to height variation than to width reduction. This will be explained in detail later in the text, but it highlights the importance of the scaling parameters L_p and α_0.

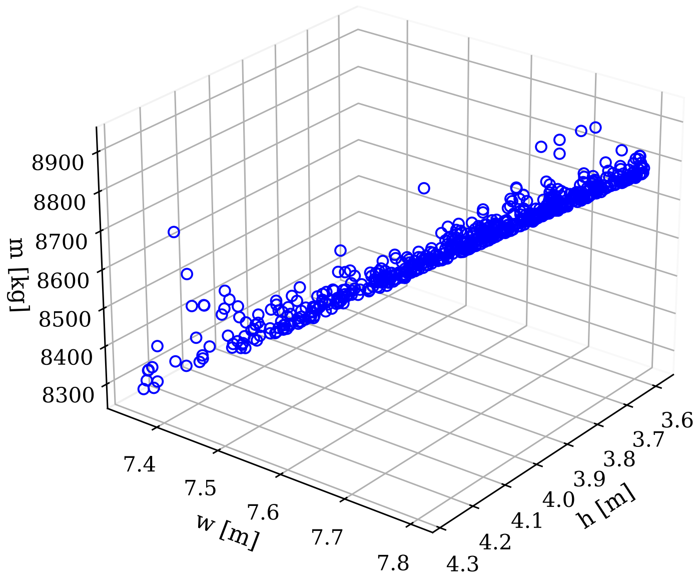

Figure 5.2: CMOPSO average Pareto front formed in 3D objective space for 10 runs

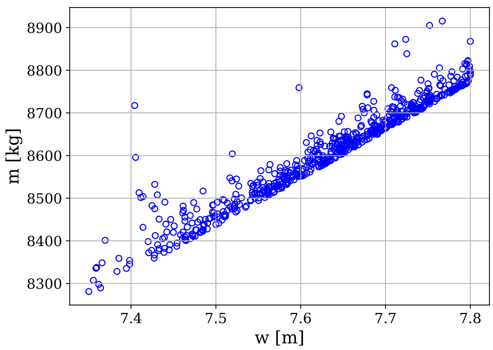

(a) 2D projection : mass vs width

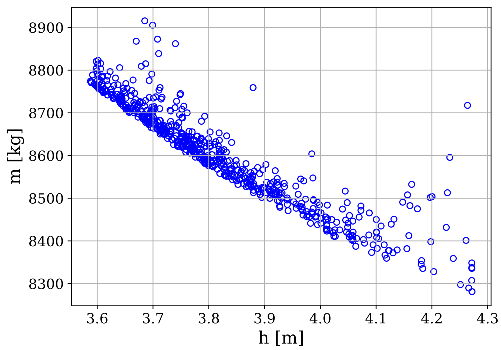

(b) 2D projection : mass vs height h

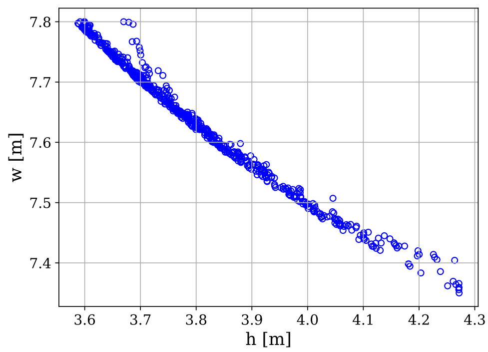

(c) 2D projection : width vs height

Figure 5.3: CMOPSO Pareto Front 2D projection

Figure 5.4 illustrates the statistical distribution of the search variables for 10 runs. It can be seen that the mean and the median are very close to each other, which is the typical signature of a normal distribution. This indicates the absence of outliers which is a good sign of stability of the algorithm as the results are not influenced by its stochasticity. Furthermore, the algorithm exhibits a narrow distribution regarding the values of t and α_0. These are concentrated around a single value of 14 µm for the thickness t and 14 ° for the initial opening angle of the pouch. L_p and w exhibit a larger standard deviation, indicating greater volatility in their behavior.

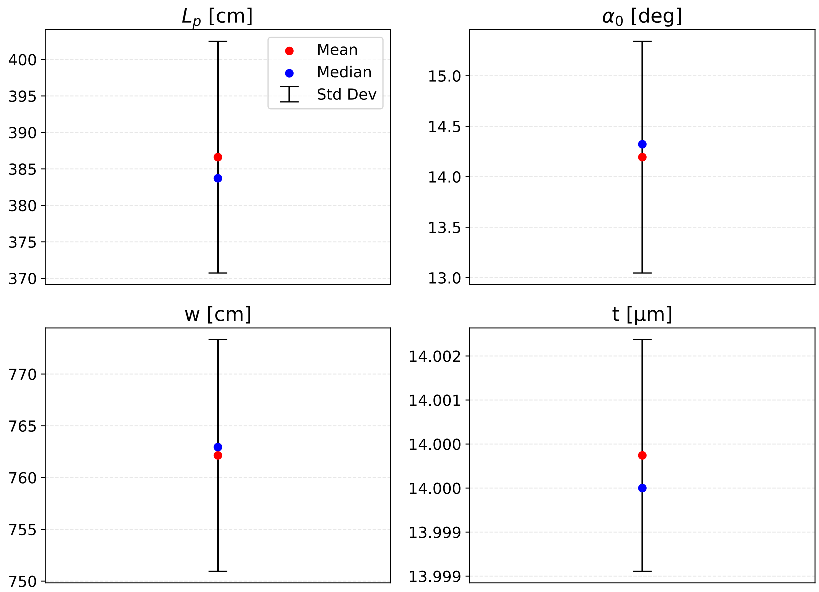

Figure 5.4: Statistical distribution of the optimization variables: L_p,α_0,w,t. The black bar represents the standard deviation , the red point is the mean and the blue one is the median of the results for 10 runs (enhanced with the help of AI)

5.5 Comparison and interpretation

The first metric used to compare these algorithms is the computation time. The GS algorithm takes 135.74 seconds to run while the CMOPSO algorithm only takes 1.96 seconds making it 68 times faster than grid search. This difference can be explained by the fact that the run time of the grid search depends heavily on the magnitude of the steps used. Larger steps allow for a gain in computational speed as there are less solutions that need to be evaluated. However, this might result in a coarse search for which few to no solution could be found. Conversely, small steps ensure that all possible solutions to the problem are found at the expense of running time. Table 5.2 shows a trade off for each step value corresponding to existing HASEL dimensions for L_p,w and t. To each value of α_0 corresponds a volume of oil filling the pouch. Therefore, the step value of α_0 was experimentally fixed to 5° to ensure covering a wide range of pouch filling.

Both algorithms produce results that are not feasible in practice. In particular, the mass appears to increase significantly with the dimensions h and w. Notably, Fig. 5.1 shows a quadratic relationship between the mass and the height of the pouch, whereas Eq. 4.2 establishes a linear relationship between m and h. However, using Eq. 2.5 the cross section of the pouch can be rewritten to highlight h using Eq. 2.4:

$$A = \frac{1}{2}{L_p}^2 \left(\frac{\alpha_0 - \sin(\alpha_0)\ \cos(\alpha_0)}{\alpha_0^2}\right) = \frac{1}{2}\left(\frac{h\ \alpha_0}{\sin(\alpha_0)}\right)^2 \left(\frac{\alpha_0 - \sin(\alpha_0)\ \cos(\alpha_0)}{\alpha_0^2}\right) \tag{5.1}$$

providing insight into how the total mass of the actuator is heavily dependent on the geometry and specifically h. Moreover, by substituting numerical values into Eq. 4.2 we can observe that $m_{\text{plastic}} \ll m_{\text{oil}}$ highlighting the fact that the main component of the total mass is the oil volume :

$$\begin{aligned} m_{\text{plastic}} &= 2\ t\ w\ h\ \rho_p = 0.935[\text{kg}] \\ m_{\text{oil}} &= A\ w\ \rho_o = 8714.22[\text{kg}] \\ m_{\text{tot}} &= m_{\text{plastic}} + m_{\text{oil}} = 8715.15[\text{kg}] \end{aligned} \tag{5.2}$$

where we used the data of the Pareto point (in red in Fig. 5.1).

The nature and magnitude of these results can be explained by the over-constrained nature of the problem. Specifying BOPP as the plastic film material and limiting the voltage range to 8 kV reduces the impact of the Maxwell stress tensor term in Eq.2.13, resulting in forces of lower magnitude and a less steep slope, corresponding to a lower stiffness range. To compensate for this effect, both algorithms favor unrealistic geometric dimensions in order to satisfy the conditions on voltage and stiffness. Indeed, as described by Eq. 2.13, the force of the system increases linearly with w and is inversely proportional to the thickness t. Consequently, the algorithms tend to favor small values of t and large values of w. Regarding h, or equivalently the arc length of the pouch L_p, it scales linearly with the contraction x. In the specifications, the rotation limit $\Delta\theta_{\text{max}}$ was set to 80°. This gives us a maximum rotational contraction $x_{\text{max rot}}$ equal to $2\ r\ \Delta\theta_{\text{max}} = 0.055$m. Using Eq. 3.10 this translates to a free stroke $x_f = 0.111$ m which is ten times greater than what a standard HASEL is capable of producing.

The following section proposes a more detailed analysis of the force-length curve and how it varies as a function of the parameters L_p, α_0, w, t and the Maxwell stress tensor $\epsilon_r\epsilon_0 V^2$.

More specifically, by investigating how these variations influence the slope of the characteristic curve we will be able to get a clearer understanding of how they affect the stiffness range we are able to achieve as the slope represents the linear stiffness of the muscle. As stated in Eq. 3.9, this stiffness is related to the angular stiffness through the square of the radius r.

The choice of a relative permittivity ϵ_r and its associated breakdown voltage will also be discussed. The aim of these analyses is to observe how the parameters L_p, α_0, w , t and ϵ_r affect the specifications and to explain why the specifications of Table 5.1 are unattainable with current HASEL technology.

5.6 Sensitivity analysis

5.6.1 $F - x$ characteristic

Several F-x characteristic curves are shown in Fig. 5.5. The graph in the upper left corner shows the reference characteristic in blue, which is kept constant across the four sub-graphs. The other plots vary a specific parameter while keeping the others at their reference values. More specifically, several characteristics were examined by arbitrarily varying the voltage V, the width w and the thickness t of the pouch, while maintaining the orders of magnitude determined by the two algorithms.

Equation 2.13 has already shown how the force varies as a function of these different parameters. However, the graphs also illustrate how the stiffness varies with these parameters. In general, the slope of the characteristic becomes steeper as the parameters increase, with the exception of the sub-graph representing the different pouch thicknesses t, for which the opposite effect is observed. This translates to an increase in the linear stiffness of the muscle and thus of the angular stiffness R of the joint.

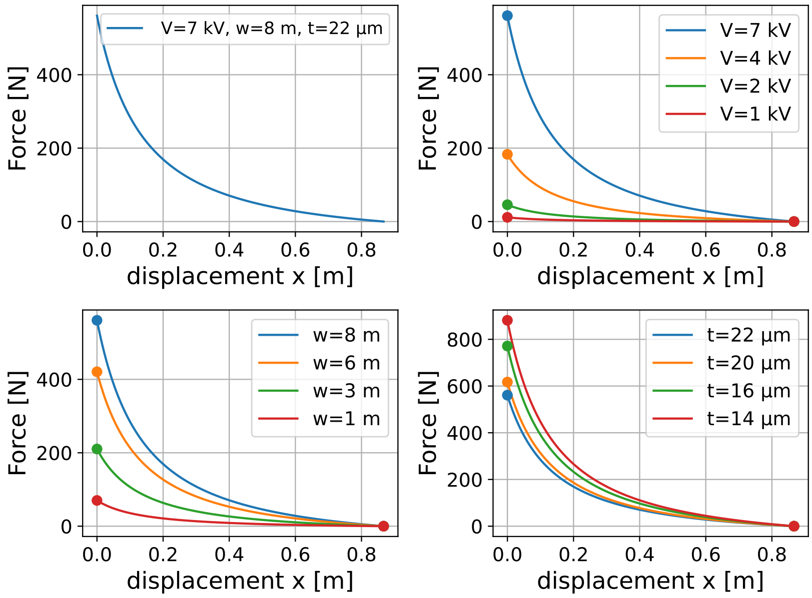

Figure 5.5: $F - x$ characteristic study for multiple values of w , t and V with $L_p =$ 4m,$\alpha_0 = 30$ °

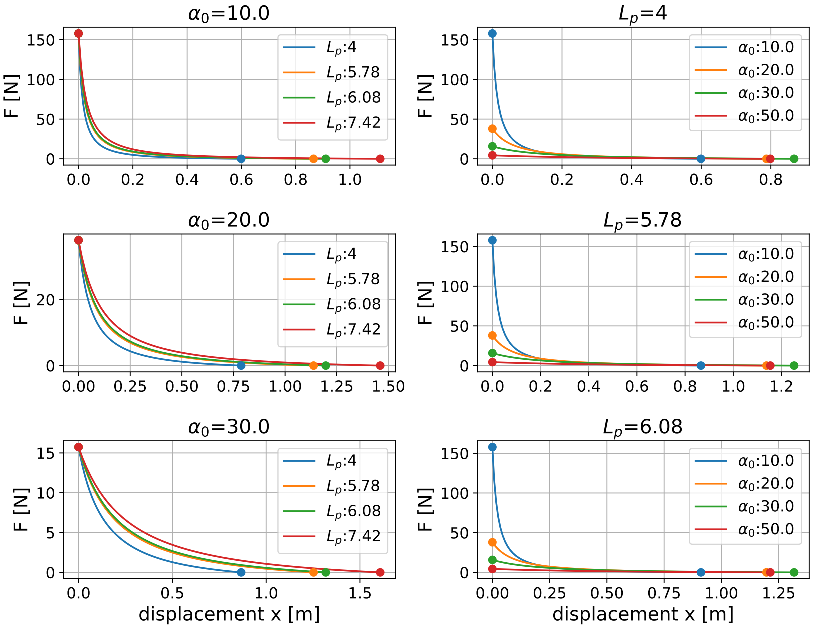

Figure 5.6: $F - x$ characteristic study for multiple values of L_p and α_0 with $w = 7$m, $t = 14\mu$m, $V = 1$kV

Figure 5.6 illustrates different characteristics force-displacement $(F - x)$ for different values of L_p and α_0. The impact of L_p on the characteristic curve is a linear scaling of the displacement x, which causes the curve to flatten and translates to an overall lower actuator stiffness. This observation can also be seen from a mathematical point of view. Taking Eq. 2.7 and making L_p explicit , we obtain:

$$x(\alpha) = L_p \left[\frac{\sin(\alpha_0)}{\alpha_0} - 1 + \frac{\alpha}{\alpha_0} \left(1 - \frac{\sin(\alpha)}{\alpha} \right) \sqrt{\left(\frac{\alpha_0 - \sin(\alpha_0)\cos(\alpha_0)}{\alpha - \sin(\alpha)\cos(\alpha)} \right)} \right] \tag{5.3}$$

where the linear relationship between x and L_p is clearly emphasized.

Regarding α_0, it has an impact on both the force and displacement. Indeed, α_0 regulates the initial force F_0 of the actuator. Observing the right graphs of Fig. 5.6 the results clearly indicate that as α_0 increases, the force F_0 obtained for $x(\alpha = \alpha_0) = 0$ decreases leading to a global lower characteristic. Regarding its effect on the stroke x it appears that a maximal free stroke $x_{f\ \max}$ is associated with a certain value of α_0. This can be confirmed by plotting this maximal free stroke for several values of α_0 as it is done in Fig. 5.7. The stroke seems to reach a peak value for $\alpha_0 \cong 35°$. This observation is similar to what Kellaris et al. observed in their work [16] for the electrodes ratio f_e i. e. the surface of the pouch covered with electrodes on the total surface of the pouch. In particular, using the equation linking α_0 to f_e we can deduce:

$$f_e = \frac{L_e}{L_p} = 1 - \sqrt{\frac{\pi}{2} \left(\frac{\alpha_0 - \sin(\alpha_0)\ \cos(\alpha_0)}{\alpha_0^2} \right)} = 0.22 \tag{5.4}$$

which corresponds to the value obtained by Kellaris. The arc length L_e ensuring the maximum stroke $x_{f\ \max}$ corresponds therefore to 20 % of the total arc length L_p of the pouch. This last result is only valid assuming optimum filling as Eq. 5.4 was derived based on this hypothesis.

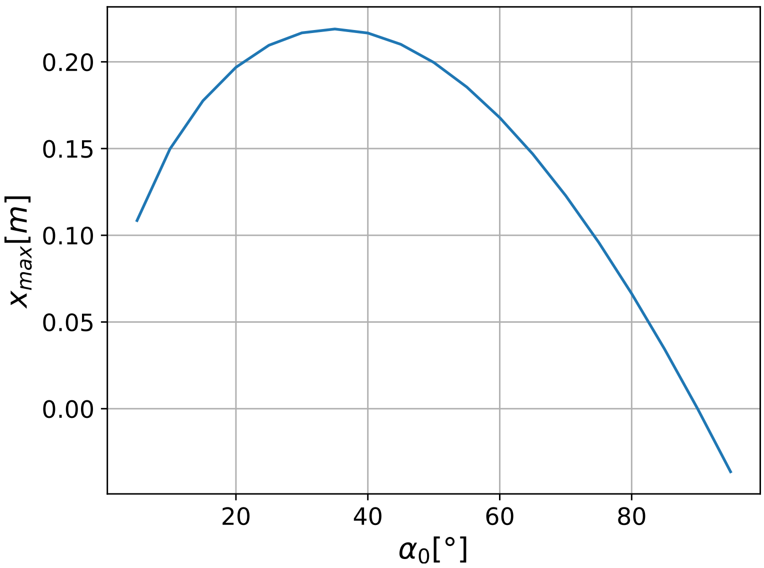

Figure 5.7: Maximal free stroke evolution as a function of α_0

This can also be interpreted from a physical point of view. As α_0 increases, the pouch is more filled and approaches the optimum filling state where $\alpha_f = \frac{\pi}{2}$. Therefore, it limits the stroke x as the range that α can take is reduced. Similarly, for low values of α_0, the actuator is not able to contract as the blocking force F_b is insufficient to zip the electrodes together.

5.6.2 Relative permittivity

Another key factor influencing our results is the selected material. So far, we have assumed that we are working with BOPP. As previously stated, this material has a relative permittivity $\epsilon_r = 2.2$ and a breakdown voltage of 8 kV for a thickness of 14 µm. It also restricts the thickness range to $t \in [14, 50]$µm. This material was chosen because it is the standard sealing material used in practice. It has relatively good mechanical properties, is durable and possesses exceptional electrical properties. Furthermore, it is easy to manufacture while remaining affordable [25]. Its main drawback lies in its low relative permittivity.

Other materials specialized for high-voltage applications have been developed, such as Polyvinylidene Fluoride PVDF, which has a relative permittivity of $\epsilon_r = 50$ and a breakdown voltage of 6 kV at a thickness of 10 µm[10, 25]. With a relative permittivity twenty times greater than that of BOPP, this material allows for the application of much greater forces. The disadvantage of this material is that it has poor mechanical properties, which makes the actuator more fragile and more prone to breaking. Furthermore, its fabrication is more complex than that of BOPP.

Theoretically, increasing ϵ_r and reducing t results in greater blocking forces. This could allow the system to meet the stiffness and torque requirements without driving the algorithm toward disproportionate geometric dimensions and excessive masses. However, Fig. 5.8 and the 2D projections in Fig. 5.9 present the results we obtained using a PVDF plastic film (by modifying the lower thickness limit to 10 µm and the maximum voltage to 6 kV while keeping the other specifications, variables and constraints constant).

Although the mass, height, and width are significantly reduced, the overall results remain unfeasible, leading us to conclude that the specifications we hoped to achieve by using HASEL muscles in an antagonist configuration are overly restrictive. The following section proposes a reverse-engineering approach to review these specifications and identify more reasonable ones, taking into account the standard dimensions of HASEL muscles.

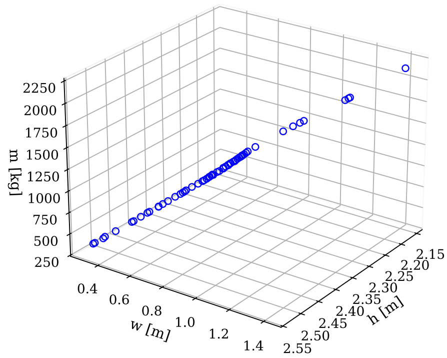

Figure 5.8: CMOPSO Pareto front using PVDF with $\epsilon_r = 50$

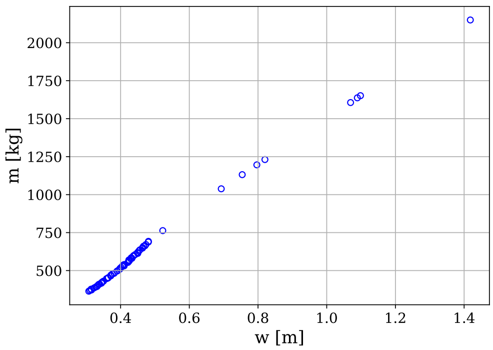

(a) 2D projection : mass vs width

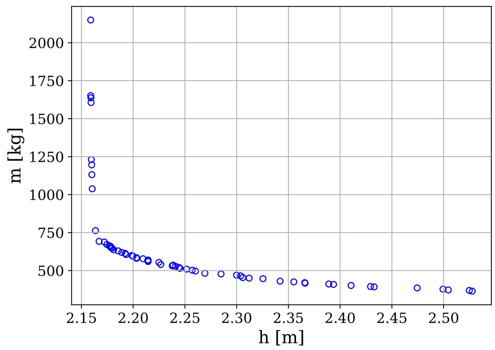

(b) 2D projection : mass vs height h

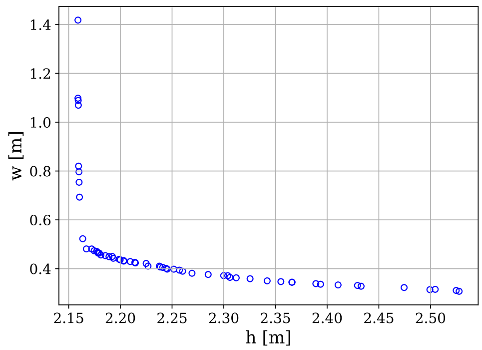

(c) 2D projection : width vs height

Figure 5.9: CMOPSO Pareto front 2D projection using PVDF with $\epsilon_r = 50$

5.7 Specifications for existing HASEL actuators

Based on the insights gained regarding parameters influence on the $F-x$ characteristic, a reverse engineering approach is applied to identify specifications that currently existing HASEL technology is able to satisfy. To do so, we consider the following parameters extracted from the annex files in [16]:

L_p [mm]	w [mm]	t [µm]	liquid fill [ml]	ϵ_r [-]
20	90	18	3.1	2.2

Table 5.3: Peano-HASEL actuator properties[16]

The liquid fill of the pouch was computed assuming optimum filling, i.e. assuming that the bottom half of the actuator forms a perfect cylinder under full actuation. Knowing the oil volume and the width of the actuator, the cross-section A can be computed to finally deduce the initial opening angle α_0 of the pouch using a non-linear solver. The corresponding value is 46.5°. Using this data, we can calculate the blocking force and free stroke of this muscle, assuming an operating voltage of 8 kV:

$$\begin{aligned} F_b &= 41[\mathrm{N}] \\ x_f &= 3[\mathrm{mm}] \end{aligned} \tag{5.5}$$

This allows us to calculate the maximum angular amplitude we can cover for the same radius as the one found by Crevecoeur using equation 3.10:

$$\frac{x_f}{2\ r} \geq \Delta\theta_{\max} \tag{5.6}$$

This corresponds to an angular range of [-4,4]°, which is 20 times smaller than the range we wanted to cover. Regarding the stiffness range, we can reverse the reasoning presented earlier in Chapter 3 to find the angular stiffness corresponding to the characteristic defined by the geometry of Table 5.4. The resulting stiffness range spans from 4 to 21 Nm/rad, which is roughly 10 times higher than the target specifications. However, special attention should be paid to the physical meaning of this value. Although muscle models typically exhibit positive stiffness to ensure joint stability,as seen previously, the slope of the $F-x$ curve is negative yielding a negative linear and angular stiffness. This leads to an unstable system behavior. The range described above is therefore considered in absolute terms. To this range corresponds a torque τ equal to 0.16 Nm which is again lower than the inital target torque of 2 Nm specified by Crevecoeur.

Similar to Table 5.1, we can therefore compile the following table summarizing the specifications for the muscle described above:

Specifications	
$[R_{\min}, R_{\max}]$	[4,21] [Nm/rad]
τ	0.16 [Nm]
$[\Delta\theta_{\min}, \Delta\theta_{\max}]$	[-4,4] [°]
$\Delta\theta$	0 [°]
r	40[mm]

Table 5.4: Specifications obtained for existing HASEL technology given an operating point $(\tau, \Delta\theta)$

Chapter 6

Discussion and possible improvements

This final chapter provides a discussion on the algorithms implemented as well as on current HASEL technology and its limitations. Next, the boundaries and assumptions of the analytical model used to derive the algorithms are addressed. Finally, a conclusion summarizes the key elements developed in this master thesis.

6.1 Methods Implemented

Regarding the grid search method, several improvements can be made to enhance both the computational speed and the results obtained. First, the method implemented is using four constant steps related to the four geometrical variables (L_p, α_0, w, t). This forces the algorithm to sweep across the entire search space at a constant rate. To improve this rate, we could use variable steps performing in a first place a coarse space search and then making a second sweep refining the steps in the areas of the space showing the majority of solutions. This would ensure a faster computational rate while maintaining the exhaustiveness of the algorithm. Another improvement that can be done is the optimization of the data structure. The algorithm is using a CSV file structure to store the different results. This requires writing solutions in a CSV file whenever they meet the constraints discussed previously. This operation of opening and writing in a csv files for each solution costs a lot of computation time. Using alternate data structure such as dictionary in which we would temporary store the solution before writing them once the search is over would be more efficient.

For the heuristic algorithm we presented the CMOPSO. While requiring careful tuning on hyper-parameters like the mutation rate or the weights linked to the position update, this algorithm ensures convergence toward a Pareto Front (or at least local optima). The drawback of this algorithm is the competition mechanism described in Chapter 4. As mentioned before, this mechanism divides the population in two sides the winners and the losers. While the losers update their positions based on the winners positions, the winners themselves remain stationary during that iteration decelerating the exploration of the search space and the overall algorithm. Moreover, depending on the tuning of the hyper-parameters, the losers might converge too rapidly towards the winners jumping over local or global optima. Hyperparameters tuning require thus an extra care in order to avoid non desired behaviors. More traditional algorithms like NSGA-II could have been used even though they are slower than CMOPSO.

6.2 HASEL limitations and future improvements

As described in Chapter 5, the HASEL technology suffers from several limitations such as high voltage requirements and moderate strains achievable. Kellaris et al. were able to obtain a contraction x equal to 15 % of the total length of the actuator [16]. The decreasing shape of the force displacement $(F - x)$ characteristic heavily limits the performance of the actuators.

This performance can be enhanced using series and parallel configurations presented in Section 2.4. In particular, the series configuration reduces the total mass m_{tot} of the actuator while the parallel configuration scales up the output force F. However, both configurations require design trade-offs as the number of pouches increases rapidly.

Additionally, the manufacturing processes were not discussed but need to be taken into account as they could introduce parasitic effects such as air bubbles in the pouch. Moreover, the availability of the materials used for the fabrication of HASELs makes them more suited for industrial production rather than specific uses. The latter shows that even if it is possible to meet the target specifications, it may be difficult to find the adequate materials or film thickness t for example.

To compensate for HASELs limitations, Kazemipour et al. proposed adding electrostatic clutches in series with the HASEL actuators [14]. These clutches were used for the extension of the muscle while the contraction was handled with HASELs. They showed good performance capable of achieving an angular range of 150°. Moreover, since the clutches do not require a significant voltage to be actuated ($\sim$ 100 V) they can use the same power supply as the HASELs.

6.3 Limitations of the analytical model

As mentioned before, all results produced were based on the analytical model developed by Kellaris and his team [16]. This model is based on several hypotheses presented in Chapter 2 and recalled below:

1. The dielectric film is inextensible and its bending is neglected
2. The mechanical energy stored in the actuator is neglected
3. The only electrical energy contributing to the total free energy of the system is the one coming from the electrodes zipping
4. Optimum filling allowing for the maximal strain and deformation of the pouch to $\alpha_f = \frac{\pi}{2}$

Therefore, it does not account for all the physical effects that can affect the performance of HASEL actuator. For example, depending on the load and material used, the force that the actuator is sustaining could deform the shell plastically. Other effects such as the non-uniform zipping of the pouch or parasitic air bubbles coming from manufacturing processes were also neglected. In particular, these air bubbles influence the permittivity inside the shell and can lead to the formation of electric arc. Moreover, air being more compressible than oil, they diminish the hydraulic pressure within the shell. Additionally, this model ignores the wear of the electrodes and material fatigue that can have negative effects on the performances over long term use.

By neglecting the internal mechanical energy of the actuator, the balance of the total free energy U_t slightly overestimates the force F produced by the actuator.

The Optimum-filling hypothesis states that the pouch is fully deformed with a free angle $\alpha_f = \frac{\pi}{2}$ when the electrodes are fully zipped. However, as seen before, in practice deviations from this ideal configuration lead to sub-optimal behavior. For instance, if the pouch reaches the fully-deformed state when the electrodes are not yet entirely zipped, this impacts the total stroke x achievable as the angle α cannot reach its maximum value.

6.4 Conclusion

This master's thesis addressed the dimensioning of HASELs pouches for an antagonistic application. Following a literature review of soft actuator technologies with particular emphasis on HASELs artificial muscles, their distinct geometries, operating principles and the analytical model developed by Kellaris et al. for Peano-HASEL actuators were examined in detail. Then, the antagonistic configuration was formally defined, highlighting its divergence from biological inspiration and establishing its constraints and its specifications. Following that, two algorithms were implemented: a Grid Search GS algorithm, providing discrete and exhaustive coverage of the solution space, and a Competitive Multi-Objective Particle Swarm Optimization CMOPSO algorithm offering a continuous heuristic approach optimizing the objective vector F.

Next, examination of the results revealed that over-restrictive constraints significantly limited the number of viable solutions. An analysis of the $F-x$ characteristic highlighted how the geometry of the pouch and its material influence the specifications. Conveniently, the existence of a trade-off between operating voltages and geometric dimensions was established.

Afterwards, several ways to improve the results were proposed. These included the consideration of alternative materials, such as PVDF, for the fabrication of the shell enabling higher closing force and dielectric breakdown voltage. Furthermore, specifications for existing HASEL technology were formulated. Finally, a discussion regarding the work conducted, its limitations and some areas for improvement concluded this master thesis.

Bibliography

[1] Eric Acome, Shane K Mitchell, TG Morrissey, MB Emmett, Claire Benjamin, Madeline King, Miles Radakovitz, and Christoph Keplinger. Hydraulically amplified self-healing electrostatic actuators with muscle-like performance. *Science*, 359(6371):61–65, 2018.

[2] Norazam Aliman, Rizauddin Ramli, and Mohammad Soleimani Amiri. Actuators and transmission mechanisms in rehabilitation lower limb exoskeletons: a review. *Biomedical Engineering / Biomedizinische Technik*, 69(4):327–345, August 2024.

[3] Yue Cao, Yuming Li, Wenbin Lu, Sunlong Li, Zheng Mao, Zhiwei Jiang, Ying Wang, Weipeng Lu, Qing He, Liqun Zhao, Cihui Liu, Xuguang Li, and Di Yu. Emerging magnetic-responsive hydrogel actuators with anisotropic shape for intracardiovascular directional motion. *Chemical Engineering Journal*, 499:156382, November 2024.

[4] Chin-Tai Chen and Yang-Xin Zhang. Integrated design and manufacturing of a soft robotic glove with piezoresistive sensors. *Sensors and Actuators A: Physical*, 372:115349, July 2024.

[5] Bret Contreras. *Bodyweight Strength Training Anatomy*, chapter 2: Arms, page 19. Human Kinetics, Champaign, IL, 2014. Anatomical illustration of the Biceps brachii, Brachialis, and Brachioradialis.

[6] Frédéric Crevecoeur and Stephen H. Scott. Beyond Muscles Stiffness: Importance of State-Estimation to Account for Very Fast Motor Corrections. *PLOS Computational Biology*, 10(10):e1003869, October 2014.

[7] Frank Daerden, Dirk Lefeber, et al. Pneumatic artificial muscles: actuators for robotics and automation. *European journal of mechanical and environmental engineering*, 47(1):11–21, 2002.

[8] K. Deb, A. Pratap, S. Agarwal, and T. Meyarivan. A fast and elitist multiobjective genetic algorithm: NSGA-II. *IEEE Transactions on Evolutionary Computation*, 6(2):182–197, April 2002.

[9] Vigilio Fontanari. Biomechanics of the elbow 2025-26. Lecture notes, University of Trento, 2025. Course: Biomechanics of articular joints. Academic year 2025-2026.

[10] Sahil Gupta, Xuepei Yuan, T. C. Mike Chung, S. Kumar, M. Cakmak, and R. A. Weiss. Effect of Hydroxyl-Functionalization on the Structure and Properties of Polypropylene. *Macromolecules*, 46(14):5455–5463, July 2013.

[11] Ehsan Hajiesmaili and David R. Clarke. Dielectric elastomer actuators. *Journal of Applied Physics*, 129(15):151102, April 2021.

[12] Ronald Van Ham, Thomas G. Sugar, Bram Vanderborght, Kevin W. Hollander, and Dirk Lefeber. Compliant actuator designs. *IEEE Robotics & Automation Magazine*, 16(3):81–94, September 2009.

[13] N. Hogan. Adaptive control of mechanical impedance by coactivation of antagonist muscles. *IEEE Transactions on Automatic Control*, 29(8):681–690, August 1984.

[14] Amirhossein Kazemipour, Ronan Hinchet, and Robert K Katzschmann. Stretchable electrohydraulic artificial muscle for full motion ranges in musculoskeletal antagonistic joints. In *2025 IEEE International Conference on Robotics and Automation (ICRA)*, pages 6976–6982. IEEE, 2025.

[15] Nicholas Kellaris, Vidyacharan Gopaluni Venkata, Garrett M. Smith, Shane K. Mitchell, and Christoph Keplinger. Peano-HASEL actuators: Muscle-mimetic, electrohydraulic transducers that linearly contract on activation. *Science Robotics*, 3(14):eaar3276, January 2018.

[16] Nicholas Kellaris, Vidyacharan Gopaluni Venkata, Philipp Rothemund, and Christoph Keplinger. An analytical model for the design of Peano-HASEL actuators with drastically improved performance. *Extreme Mechanics Letters*, 29:100449, May 2019.

[17] Soo Jin Adrian Koh, Christoph Keplinger, Rainer Kaltseis, Choon-Chiang Foo, Richard Baumgartner, Siegfried Bauer, and Zhigang Suo. High-performance electromechanical transduction using laterally-constrained dielectric elastomers part I: Actuation processes. *Journal of the Mechanics and Physics of Solids*, 105:81–94, August 2017.

[18] Jiangyu Lan, Yinggang Xie, Guangjun Liu, and Manxin Cao. A multi-objective trajectory planning method for collaborative robot. *Electronics*, 9(5):859, 2020.

[19] Cecilia Laschi, Matteo Cianchetti, Barbara Mazzolai, Laura Margheri, Maurizio Follador, and Paolo Dario. Soft Robot Arm Inspired by the Octopus. *Advanced Robotics*, 26(7):709–727, January 2012. _eprint: https://doi.org/10.1163/156855312X626343.

[20] Wei Liang, Hao Liu, Kunyang Wang, Zhihui Qian, Luquan Ren, and Lei Ren. Comparative study of robotic artificial actuators and biological muscle. *Advances in Mechanical Engineering*, 12(6):1687814020933409, June 2020.

[21] Jianhua Liu, Yi Mei, and Xiaodong Li. An analysis of the inertia weight parameter for binary particle swarm optimization. *IEEE Transactions on Evolutionary Computation*, 20(5):666–681, October 2016.

[22] A.M Oosterwijk, M.K Nieuwenhuis, C.P van der Schans, and L.J Mouton. Shoulder and elbow range of motion for the performance of activities of daily living: A systematic review. *Physiotherapy Theory and Practice*, 34(7):505–528, July 2018. _eprint: https://doi.org/10.1080/09593985.2017.1422206.

[23] Osura Perera, Ranjith Liyanapathirana, Gaetano Gargiulo, and Upul Gunawardana. A Review of Soft Robotic Actuators and Their Applications in Bioengineering, with an Emphasis on HASEL Actuators' Future Potential. *Actuators*, 13(12):524, December 2024.

[24] Panagiotis Polygerinos, Nikolaus Correll, Stephen A. Morin, Bobak Mosadegh, Cagdas D. Onal, Kirstin Petersen, Matteo Cianchetti, Michael T. Tolley, and Robert F. Shepherd. Soft Robotics: Review of Fluid-Driven Intrinsically Soft Devices; Manufacturing, Sensing, Control, and Applications in Human-Robot Interaction. *Advanced Engineering Materials*, 19(12):1700016, 2017. _eprint: https://advanced.onlinelibrary.wiley.com/doi/pdf/10.1002/adem.201700016.

[25] Philipp Rothemund, Nicholas Kellaris, Shane K. Mitchell, Eric Acome, and Christoph Keplinger. HASEL Artificial Muscles for a New Generation of Lifelike Robots—Recent Progress and Future Opportunities. *Advanced Materials*, 33(19):2003375, 2021. _eprint: https://advanced.onlinelibrary.wiley.com/doi/pdf/10.1002/adma.202003375.

[26] R. Shadmehr and F. A. Mussa-Ivaldi. Adaptive representation of dynamics during learning of a motor task. *Journal of Neuroscience*, 14(5):3208–3224, May 1994.

[27] Mei-Ping Song and Guo-Chang Gu. Research on particle swarm optimization: a review. In *Proceedings of 2004 International Conference on Machine Learning and Cybernetics*, volume 4, pages 2236–2241 vol.4, August 2004.

[28] Raphaël Veithen. Peano-hasel actuators: Design of tools to manufacture peano-hasel actuators and demonstrator using their properties. Mémoire de master [120] en ingénierie électromécanique, École polytechnique de Louvain, Université catholique de Louvain, Louvain-la-Neuve, Belgique, Juin 2025. Promoteur : Renaud Ronsse. Lecteurs : Bruno Dehez, Thomas Pomponio.

[29] Michael Wehner, Ryan L Truby, Daniel J Fitzgerald, Bobak Mosadegh, George M Whitesides, Jennifer A Lewis, and Robert J Wood. An integrated design and fabrication strategy for entirely soft, autonomous robots. *nature*, 536(7617):451–455, 2016.

[30] Curt Woodward. Soft Robotics gets $3 million amid demand for its octopus-inspired grippers. *BetaBoston (The Boston Globe)*, December 2015. Accessed: 2026-05-31.

[31] Oncay Yasa, Yasunori Toshimitsu, Mike Y. Michelis, Lewis S. Jones, Miriam Filippi, Thomas Buchner, and Robert K. Katzschmann. An Overview of Soft Robotics. *Annual Review of Control, Robotics, and Autonomous Systems*, 6(Volume 6, 2023):1–29, May 2023.

[32] Jun Zhang, Jun Sheng, Ciarán T. O'Neill, Conor J. Walsh, Robert J. Wood, Jee-Hwan Ryu, Jaydev P. Desai, and Michael C. Yip. Robotic Artificial Muscles: Current Progress and Future Perspectives. *IEEE Transactions on Robotics*, 35(3):761–781, June 2019.

[33] Xingyi Zhang, Xiutao Zheng, Ran Cheng, Jianfeng Qiu, and Yaochu Jin. A competitive mechanism based multi-objective particle swarm optimizer with fast convergence. *Information Sciences*, 427:63–76, February 2018.

[34] Xin Zhao, Gangqiang Tang, Dong Mei, Chun Zhao, Lijie Li, and Yanjie Wang. Stimuli-responsive actuators in water environment: a review and future research agenda. *International Journal of Extreme Manufacturing*, 7(2):8,12, December 2024.

UNIVERSITÉ CATHOLIQUE DE LOUVAIN
École polytechnique de Louvain
Rue Archimède, 1 bte L6.11.01, 1348 Louvain-la-Neuve, Belgique | **www.uclouvain.be/epl**